

Dissolution and Recrystallization Behavior of Li_3PS_4 in Different Organic Solvents

Kerstin Wissel^{a,*}, Luise M. Riegger^{b,c}, Christian Schneider^d, Aamir I. Waidha^a, Theodosios Famprikis^e, Yuji Ikeda^f, Blazej Grabowski^f, Robert E. Dinnebier^d, Bettina V. Lotsch^{d,g}, Jürgen Janek^{b,c}, Wolfgang Ensinger^a and Oliver Clemens^h

^a Technical University of Darmstadt, Institute for Materials Science, Materials Analysis, Alarich-Weiss-Straße 2, 64287 Darmstadt, Germany

^b Justus-Liebig-University Gießen, Institute for Physical Chemistry, Heinrich-Buff-Ring 17, 35392 Gießen, Germany

^c Justus-Liebig-University Gießen, Center for Materials Research (ZfM), Heinrich-Buff-Ring 17, 35392 Gießen, Germany

^d Max Planck Institute for Solid State Research, Heisenbergstraße 1, 70569 Stuttgart, Germany

^e Delft University of Technology, Department of Radiation Science and Technology, Mekelweg 15, Delft 2629JB, The Netherlands

^f University of Stuttgart, Institute for Materials Science, Materials Design, Pfaffenwaldring 55, 70569 Stuttgart, Germany

^g Ludwig-Maximilians-Universität München, Department of Chemistry, Butenandtstraße 5-13, 81377 München, Germany

^h University of Stuttgart, Institute for Materials Science, Chemical Materials Synthesis, Heisenbergstraße 3, 70569 Stuttgart, Germany

Corresponding Author:

Dr. Kerstin Wissel

Email: kerstin.wissel@tu-darmstadt.de

Fax: +49 6151 16-21991

Abstract

Solid state batteries can be built based on thiophosphate electrolytes such as β - Li_3PS_4 . For the preparation of these electrolytes, various solvent-based routes have been reported. For recycling of end-of-life solid state batteries based on such thiophosphates, we consider the development of dissolution and recrystallization strategies for the recovery of the model compound β - Li_3PS_4 . We show that recrystallization can only be performed in polar, slightly protic solvents such as N-methylformamide (NMF). The recrystallization is comprehensively studied, showing that it proceeds via an intermediate phase with composition $\text{Li}_3\text{PS}_4 \cdot 2\text{NMF}$, which is structurally characterized. This phase has a high resistivity for the transport of lithium ions and must be removed in order to obtain a recrystallized product with a conductivity similar to the pristine material. Moreover, the recrystallization from solution results in an increase of the amorphous phase fraction next to crystalline β - Li_3PS_4 , which results in a decrease of the activation energy to 0.2 eV compared to 0.38 eV for the pristine phase.

Keywords

Thiophosphate, β - Li_3PS_4 , solvent treatment, recrystallization, N-methylformamide, recycling

1 Introduction

Inherent safety concerns related to the use of combustible liquid electrolytes and limited energy density of commercial lithium ion batteries (LIBs) have prompted the development of different next-generation battery technologies, of which all-solid-state batteries (ASSBs) utilizing solid electrolytes (SEs) are regarded to be highly promising. Various material classes (e.g. oxides, halides and sulfides) are currently investigated for their use as SE. Among these, sulfides show some of the highest room-temperature ionic conductivities (up to $\approx 10^{-2}$ S/cm).¹ Prominent examples of these sulfide SEs are Li-P-S (LPS)-based glasses or glass ceramics (e.g. $x\text{Li}_2\text{S}\cdot(100-x)\text{P}_2\text{S}_5$, $\text{Li}_7\text{P}_3\text{S}_{11}$, $\beta\text{-Li}_3\text{PS}_4$), argyrodites $\text{Li}_6\text{PS}_5\text{X}$ (X = Cl, Br, I), thio-LISICONs or $\text{Li}_{11-x}\text{M}_{2-x}\text{P}_{1+x}\text{S}_{12}$ (M = Ge, Sn, Si). $\beta\text{-Li}_3\text{PS}_4$, $\text{Li}_7\text{P}_3\text{S}_{11}$ and argyrodites can be obtained via scalable liquid-phase syntheses. For example, $\beta\text{-Li}_3\text{PS}_4$ can be synthesized when its precursors Li_2S and P_2S_5 are either dissolved or dispersed in different organic solvents. Commonly used solvents for the synthesis are e.g. acetonitrile (ACN)², diethylene glycol dimethyl ether (DEGDME)³, dimethyl carbonate (DMC)⁴, dimethoxyethane (DME)⁵, ethyl acetate (EA)⁶, ethylenediamine (EDA)⁷, N-methylformamide (NMF)⁸⁻¹⁰ or tetrahydrofuran (THF)¹¹. During the synthesis, the precipitation of Li_3PS_4 complexed with the respective solvent (e.g. $\text{Li}_3\text{PS}_4\cdot\text{ACN}$ ¹², $\text{Li}_3\text{PS}_4\cdot\text{DME}$ ⁵, $\text{Li}_3\text{PS}_4\cdot 2\text{EA}$ ⁶, $\text{Li}_3\text{PS}_4\cdot 3\text{THF}$ ¹¹) takes place. After an additional thermal treatment to remove the solvent, $\beta\text{-Li}_3\text{PS}_4$ crystallizes from these complexes.¹²

With the expected commercialization of ASSBs, sustainable battery recycling strategies will be of rising urgency. However, to date, most of the recycling research efforts focus on traditional LIBs with organic liquid electrolytes and are based on pyrometallurgical and/or hydrometallurgical processes, aiming at the recycling of the valuable metals (predominantly Ni, Co, Mn) contained in the electrode materials only. Irrecoverable losses of the liquid electrolytes and lithium lower the overall material recovery rate drastically, while the energy and cost efficiency remain low as well. As ASSBs are still under development, there is great opportunity to early on establish economically viable and efficient recycling strategies taking also sustainable battery design concepts with a focus on the recyclability of such batteries into account. Owing to the potential for solution-processing of sulfide electrolytes, sulfide-based ASSBs might offer significant potential in this respect since direct recycling concepts involving the dissolution and recrystallization of the electrolyte could be adopted.¹³ This way, the insoluble electrode materials could be separated via filtration or centrifugation from the dissolved electrolyte and processed separately. So far only little is known on the recycling of sulfide electrolytes: Tan et al.¹⁴ reported on a potential recycling strategy for thiophosphate electrolyte-based $\text{Li}|\text{Li}_6\text{PS}_5\text{Cl}|\text{LiCoO}_2$ cells employing ethanol as solvent allowing for a

separation of LiCoO_2 from the formed suspension. After the removal of the solvent $\text{Li}_6\text{PS}_5\text{Cl}$ could be recovered.

A key requirement for this recycling strategy is that the electrolyte is fully dissolvable, while avoiding a chemical degradation of the electrolyte when in solution. In this context, it has been noted that polar solvents readily solvate thiophosphate units.^{13, 15} Keeping thiophosphate units intact is essential, although it can be difficult since sulfide electrolytes show a high reactivity towards most solvents. It should be noted that dissolution strategies must be conceptually distinguished from synthesis strategies, as not precursor materials but the sulfide electrolytes have to be processed in the solvent. For $\beta\text{-Li}_3\text{PS}_4$, there is a large number of studies on solvent-based processing in the context of the preparation of active electrode coatings, composite electrodes or separator films, however, most of these studies start from the precursor Li_2S and P_2S_5 (or glassy $75\text{Li}_2\text{S}\cdot 25\text{P}_2\text{S}_5$ (mol%)) and/or use non-polar or weakly polar aprotic solvents only.¹⁶⁻²⁴ Thus, this study aims to investigate the impact of solvent treatments on $\beta\text{-Li}_3\text{PS}_4$. For this, a variety of solvents covering a broad range of physical and chemical properties is systematically screened and the solubility of $\beta\text{-Li}_3\text{PS}_4$ within them is investigated. Structural and chemical changes of the precipitated phases formed after the removal of the solvent are examined using X-ray diffraction (XRD) and Raman spectroscopy. A detailed investigation on the recrystallization behavior of $\beta\text{-Li}_3\text{PS}_4$ after complete dissolution in NMF is carried out. The formation of a previously unreported $\text{Li}_3\text{PS}_4\cdot 2\text{NMF}$ complex is observed which is determined to have a C-centered monoclinic crystal structure in the space group $C2/c$. Effects of the dissolution in NMF on the obtained materials are investigated via a combination of X-ray and neutron diffraction, Rietveld analysis, X-ray photoelectron (XPS), infrared (IR) and electrochemical impedance (EIS) spectroscopy. Morphology changes are followed using scanning electron microscopy (SEM).

2 Experimental

2.1 Material Preparation

The pristine electrolyte β -Li₃PS₄ was purchased from NEI Corporation (USA). Material handling and preparation was carried out in inert atmosphere.

To investigate the effect of a solvent treatment on β -Li₃PS₄, different organic solvents (hexane (anhydrous, Alfa Aesar), toluene (anhydrous, 99.8 %, Sigma Aldrich), tetrahydrofuran (THF, anhydrous, 99.8+ %, Alfa Aesar), ethyl acetate (EA, 99.8 %, Sigma Aldrich), 1,2-dimethoxyethane (DME, anhydrous, 99.5 %, Sigma Aldrich), acetonitrile (ACN, anhydrous, 99.8+ %, Alfa Aesar), N-methyl formamide (NMF, 99%, thermo scientific), isopropanol (i-PrOH, anhydrous, max. water 0.003 %, VWR Chemicals), ethanol (EtOH, anhydrous, max. water 0.003 %, VWR Chemicals), and methanol (MeOH, anhydrous, 99.9%, thermo scientific) were selected. This selection covers a variety of solvents that are commonly used in literature for the synthesis of β -Li₃PS₄ (i.e., THF, EA, DME, and ACN (polar, aprotic); NMF (polar, (weakly) protic), as well as other nonpolar solvents (i.e., hexane and toluene) and polar, stronger protic solvents (i.e., i-PrOH, EtOH and MeOH). The physical and chemical properties of the used solvents are summarized in Table S1. The solvents were dried over molecular sieve (3 Å, 20% m/v, Sigma-Aldrich). The molecular sieve was removed from the solvent after 72 h via filtration. To avoid any contamination from colloidal molecular sieve particles within the solvent, vacuum distillation was carried out in addition. The water contents of the solvents were determined by Karl Fischer titration (Titrator Compact C10SX, Mettler-Toledo) and are also given in Table S1. 250 mg of the electrolyte were mixed with 50 ml solvent under Ar-atmosphere. After 4 h of stirring, the Schlenk-flasks were connected to a Schlenk line and heated to 120 °C under vacuum ($p \approx 1-3 \cdot 10^{-2}$ mbar) for 4 h to remove the respective excess solvent. For ACN, DME and NMF, additional heat treatments of the obtained powders were performed at 240 °C in a vacuum oven (glass oven B-585 drying, Büchi).

For further dissolution experiments with NMF, different β -Li₃PS₄ to NMF solid-to-liquid ratios were investigated. Using a ratio of 50 mg to 1 ml and a stirring time of 30 min, 3 g of β -Li₃PS₄ were dissolved in NMF and the sample was heated to a temperature of 120 °C at a pressure of $\sim 2 \cdot 10^{-2}$ mbar for 4 h. This sample was subsequently divided into several samples and each one was heated to a temperature between 140 and 240 °C under vacuum for additional 4 h.

2.2 Characterization

2.2.1 X-ray and Neutron Powder Diffraction and Rietveld analysis

XRD patterns were recorded on a Rigaku SmartLab in Bragg-Brentano geometry with Cu K α radiation with a wavelength of 1.542 Å and a Hypix-3000 detector. Samples were measured

inside low background air-tight sample holders (Rigaku), which were sealed inside an Ar-filled glovebox.

Neutron powder diffraction (NPD) experiments were performed at the PEARL diffractometer of the Reactor Institute Delft (TU Delft, the Netherlands)²⁵. Approximately 600 mg of sample were loaded in a 6 mm diameter can made from V-Ni null-scattering alloy which was sealed airtightly using a rubber O-ring. Handling of the powder was performed in an Ar-filled glovebox. The sample can was placed in a neutron-transparent vacuum box connected to primary vacuum ($\sim 10^{-3}$ mbar). The diffractogram was measured over ~ 21 h using a wavelength of 1.667 Å selected using the (533) reflection of a Ge[511] monochromator. The instrument background determined from measurements of the empty can was subtracted from the raw diffractogram. Detector pixel normalization was performed by fitting a measurement of a PMMA rod in the same configuration.

Analysis of diffraction data was performed via the Rietveld method with the program TOPAS V.6.0. For the crystal structure determination, a coupled Rietveld analysis of X-ray and neutron powder diffraction data was performed. The instrumental intensity distribution of the XRD and NPD instruments were determined empirically from a fundamental parameter set determined using a reference scan of LaB₆ (NIST 660a) and Al₂O₃ (NIST 676a), respectively. Microstructural parameters (i.e., crystallite size and strain broadening) were refined to adjust the peak shapes.

For the determination of amorphous phase contents, the samples were mixed in a defined weight ratio with Al₂O₃ (calcinated at 1100 °C) and XRD patterns were recorded. The calculation of the respective amorphous fraction was performed using the internal standard method as implemented in TOPAS V.6.0.

2.2.2 Thermogravimetric and evolved gas analysis

To quantify the amount of solvent in Li₃PS₄·xNMF thermogravimetric analysis (TGA) was performed. Furthermore, evolved gas analysis (EGA) was performed to identify the compounds released during TG analysis. Prior to the TGA/EGA measurement, blank samples were measured to minimize buoyancy effects in the TGA and to obtain background spectra in the EGA. For the TGA measurement about 10 mg of Li₃PS₄·xNMF powder sample were loaded into an Al₂O₃ crucible and subsequently transferred into the furnace chamber. The TGA was carefully purged several times with helium to avoid atmospheric contaminates. The sample was heated with a heating rate of 10 K min⁻¹ to 300 °C (Netzsch Jupiter STA 449 F3, SiC furnace, type S thermocouple sample carrier, 70 ml min⁻¹ He (5N Air Liquid) stream). The TGA data was analyzed with the software *Proteus Analysis* (Netzsch). Sampling of the evolved exhaust gas was performed at 86 °C, 212 °C, and 278 °C. The sampled gas was transferred *via* an inert, heated line to a gas chromatograph (GC, Agilent 8890 GC System, HP-5MS UI

column with 30 m · 0.25 mm · 0.25 µm, 20:1 injection split ratio, sample inlet temperature 300 °C, He carrier with 1.2 mL min⁻¹). The GC oven was set to a constant temperature of 100 °C. After passing the GC, the separated components were detected in a mass spectrometer (MS, Agilent 5977B GC/MSD, EI mode, 230 °C ion source temperature, 150 °C quadrupole temperature). The total ion current of the GC peaks was measured. The mass spectra were analyzed by means of best matching database entries (NIST database, *MSD ChemStation Data Analysis*).

2.2.3 DFT calculations

To further support the atomic positions determined in the Rietveld analysis, structural optimization based on ab initio density functional theory (DFT) was also conducted. The optimization was done for the primitive cell including 52 atoms, where the primitive lattice vectors are $(\mathbf{a} - \mathbf{b})/2$, $(\mathbf{a} + \mathbf{b})/2$, and \mathbf{c} . The DFT calculations were performed using the VASP code.²⁶⁻²⁸ with the plane-wave basis projector augmented wave (PAW) method.²⁹ The exchange–correlation energy was obtained within the generalized gradient approximation (GGA) of the Perdew–Burke–Ernzerhof (PBE) form.³⁰ The plane-wave cutoff energy was set to 520 eV. Reciprocal spaces were sampled by a Γ -centered $6 \times 6 \times 3$ k-point mesh and the tetrahedron method with the Blöchl correction.³¹ H 1s, Li 2s, C 2s2p, N 2s2p, O 2s2p, P 3s3p, and S 3s3p orbitals were treated as the valence states. Total energies were minimized until they converged within $1 \cdot 10^{-6}$ eV per simulation cell for each ionic step. Cell volume, cell shape, and internal atomic positions were optimized so that the forces on atoms and the stress components on the unit cell became less than $1 \cdot 10^{-2}$ eV/Å and $1 \cdot 10^{-4}$ eV/Å³, respectively.

2.2.4 Scanning electron microscopy

SEM images were recorded using a secondary electron detector of a FEI Quanta 250 SEM operating at 30 keV. Prior to the measurements, a layer of Au was sputtered onto the samples.

2.2.5 Raman spectroscopy

Raman spectra were recorded with a confocal micro-Raman spectrometer Horiba HR 800 equipped with a laser wavelength of 532 nm. For calibration of the spectrometer, the 521 cm⁻¹ Stokes signal of a silicon wafer was used. Calibration measurements were performed after each measurement. Samples were measured in glass capillaries sealed under inert atmosphere.

2.2.6 Infrared spectroscopy

Fourier-transform infrared spectroscopy (FTIR) measurements were conducted on a Varian spectrometer. Samples were characterized via attenuated total reflection (ATR) using an ATR unit (Specac) equipped with a reactive sample anvil. For the sample preparation, the ATR unit was transferred into an Ar-filled glovebox, where the sample was compressed under

inert atmosphere, sealing the powder from the environment with an O-ring. To limit the duration of possible exposure to air, the measurement was conducted as quick as possible after the unit was transferred out of the glovebox.

2.2.7 X-ray photoelectron spectroscopy

XPS measurements were carried out on a PHI 5000 VersaProbe II Scanning ESCA Microprobe (Physical Electronics GmbH) with a monochromatized Al K α source (1486.6 eV). The beam had a power of 50 W and a diameter of 200 μ m. The sample surface was charge neutralized with slow argon-ions and electrons. Ar⁺ ions accelerated with 0.5 kV were used to sputter a depth profile. For the detailed spectra an analyzer pass energy of 46.95 eV, a step time of 50 ms and a step size of 0.2 eV were used. CasaXPS software (Casa Software Ltd) was used for data analysis with a Shirley-type background correction and a GL(30) line shape. Before fitting, all the peaks were calibrated to the binding energy of adventitious sp³-carbon (284.8 eV) first. To avoid detrimental surface effects the spectra were then calibrated to the binding energy of the S2p main component PS₄³⁻ at 161.7 eV.^{32, 33}

2.2.8 Electrochemical impedance spectroscopy

The conductivity of the obtained materials was measured under pressure in a CompreDrive (rhd instruments). For this, 80 to 100 mg of each powder was loaded into a measuring cell. Carbon-coated aluminum electrodes were used to ensure contact. After applying 380 MPa for 3 min, a constant pressure of 50 MPa was applied. Electrical impedance measurements were performed using an electrochemical impedance analyzer NEISYS (Novocontrol Technologies) in a frequency range between 7 MHz and 1 Hz with an amplitude of 10 mV in a temperature range between -30 and 100 °C. Received data was analyzed using the software RelaxIS3 (rhd instruments GmbH & Co. KG).

3 Results and Discussions

3.1 Solvent treatment of β -Li₃PS₄ in different organic solvents

To study the impact of a solvent treatment on β -Li₃PS₄, a selection of different organic solvents has been made based on their different physical and chemical properties (Table S1), covering a spectrum from non-polar over polar aprotic to polar protic solvents. As can be seen in Figure 1 a), only the polar protic solvents NMF, i-PrOH, EtOH and MeOH are able to form a clear solution containing a significant quantity of β -Li₃PS₄ (fixed ratios of 5 mg β -Li₃PS₄ per 1 ml of solvent were investigated). However, it should be noted that, while β -Li₃PS₄ is dissolved in less than 2 minutes in EtOH and MeOH, incomplete dissolution was observed in the case of i-PrOH and the mixture remains slightly cloudy.

For all other non-polar and polar aprotic solvents, no to negligible solubility was found leading to the presence of considerable amounts of white precipitates. A sedimentation of the particles takes place within 1 to 2 minutes showing that stable suspensions cannot be formed. The blue color of the ACN suspension points to a certain reactivity between β -Li₃PS₄ and ACN under the formation S₃⁻ radicals^{34, 35}, while colorless supernatants were observed for the other non-polar and polar aprotic solvents indicating no to minor reactions between sulfur-containing species and the solvents³⁶. The solutions with polar protic solvents have a pale-yellow color.

After the evaporation of the solvents at 120 °C and reduced pressures, the obtained precipitates were collected and X-ray diffraction and Raman spectroscopy measurements (Figure 1 b and c) were performed. The orthorhombic crystal structure of β -Li₃PS₄ is recovered for all solvents except for i-PrOH, EtOH and MeOH. It should be noted that the pristine β -Li₃PS₄ contains ~ 2 wt.% Li₂S as an impurity phase, which is also present in the recrystallized samples. The phase fraction of Li₂S remains constant in all samples.

As has been reported previously when synthesizing β -Li₃PS₄ from DME and ACN^{5, 12}, insoluble Li₃PS₄·ACN and Li₃PS₄·DME complexes are obtained when using a moderate drying temperature of 120 °C (Figure S1). Only after heating to higher temperatures, these complexes decompose and the formation of β -Li₃PS₄ takes place. A similar behavior is found for NMF suggesting the formation of a so far unknown NMF complex which also transforms to β -Li₃PS₄ at elevated temperatures. The detailed crystal structure and property characterization of this phase is described in section 3.2. For the alcohols, on the other hand, partial decomposition under the formation of Li₂S and other unknown phases and/or amorphization is observed which is also in agreement with previous studies.^{15, 37, 38} Interestingly, alcohols can be used to dissolve and recrystallize other sulfide electrolytes such as argyrodites Li₆PS₅X³⁸⁻⁴⁰ or Li₇PS₆³⁷, even though they also contain PS₄³⁻ units. For these electrolytes, the presence of excess Li₂S and/or LiX seems to play an important role for the stabilization of PS₄³⁻ units during the

dissolution process. This shows, however, that it is not necessarily possible to dissolve different electrolytes (simultaneously) in a specific solvent which could become important with respect to potential large-scale recycling considering different thiophosphate-based cell chemistries. Therefore, an additional sorting and separation step would be required. Furthermore, this illustrates that for each sulfide electrolyte which could find application in future ASSB cells the dissolution behavior has to be studied individually.

The Raman spectra are in excellent agreement with the diffraction data. The signals at $\sim 421 \text{ cm}^{-1}$ dominating the Raman spectra correspond to the symmetric stretching vibration of ortho-thiophosphate units PS_4^{3-} ^{41, 42} which are expected to be present in the samples showing the $\beta\text{-Li}_3\text{PS}_4$ structure. The decrease of this signal and the appearance of other signals (e.g. polysulfide species in the range ~ 450 to 500 cm^{-1} , $\text{P}_2\text{S}_6^{4-}$ at $\sim 390 \text{ cm}^{-1}$)³⁸ for the alcohols demonstrates that these samples decomposed significantly. This also confirms findings from previous studies.³⁶⁻³⁸

It can be concluded that only NMF dissolves $\beta\text{-Li}_3\text{PS}_4$ under the retention of the PS_4^{3-} units, making a recrystallization of the crystal structure possible. Several factors seem to play an important role: NMF is a strongly polar, weakly protic solvent containing NH bonds. The polarity and the weakly positively polarized hydrogen seem to be necessary to solvate the PS_4^{3-} anionic species. In comparison, the alcohols possess OH bonds which make them more nucleophilic. Though this leads also to the solvation of the anion, it can also cause decomposition under the formation of $\text{PS}_{4-x}(\text{OR})_x$ at the same time since PO bonds are thermodynamically more stable.¹⁵ This reaction step is irreversible and prevents the recrystallisation of $\beta\text{-Li}_3\text{PS}_4$ or Li_3PS_4 -solvent complexes. The fact that i-PrOH does not dissolve $\beta\text{-Li}_3\text{PS}_4$ completely might also show that not only the OH or NH bonds, respectively, play an important role in the dissolution process but also the size of the solvent molecules. Due to the size of i-PrOH the nucleophilic substitution reaction can be expected to be kinetically hindered¹⁵. Additionally, the polarity could play a role since NMF is much more polar than i-PrOH.

Non-polar and aprotic solvents, on the other hand, cannot break the bonding between the Li^+ cations and PS_4^{3-} anions. Consequently, this does not lead to a complete dissolution but to the formation of suspensions. From these, $\beta\text{-Li}_3\text{PS}_4$ can be recovered after the removal of the solvent, however, they do not have a significantly high solubility for solvating a considerable amount of $\beta\text{-Li}_3\text{PS}_4$.

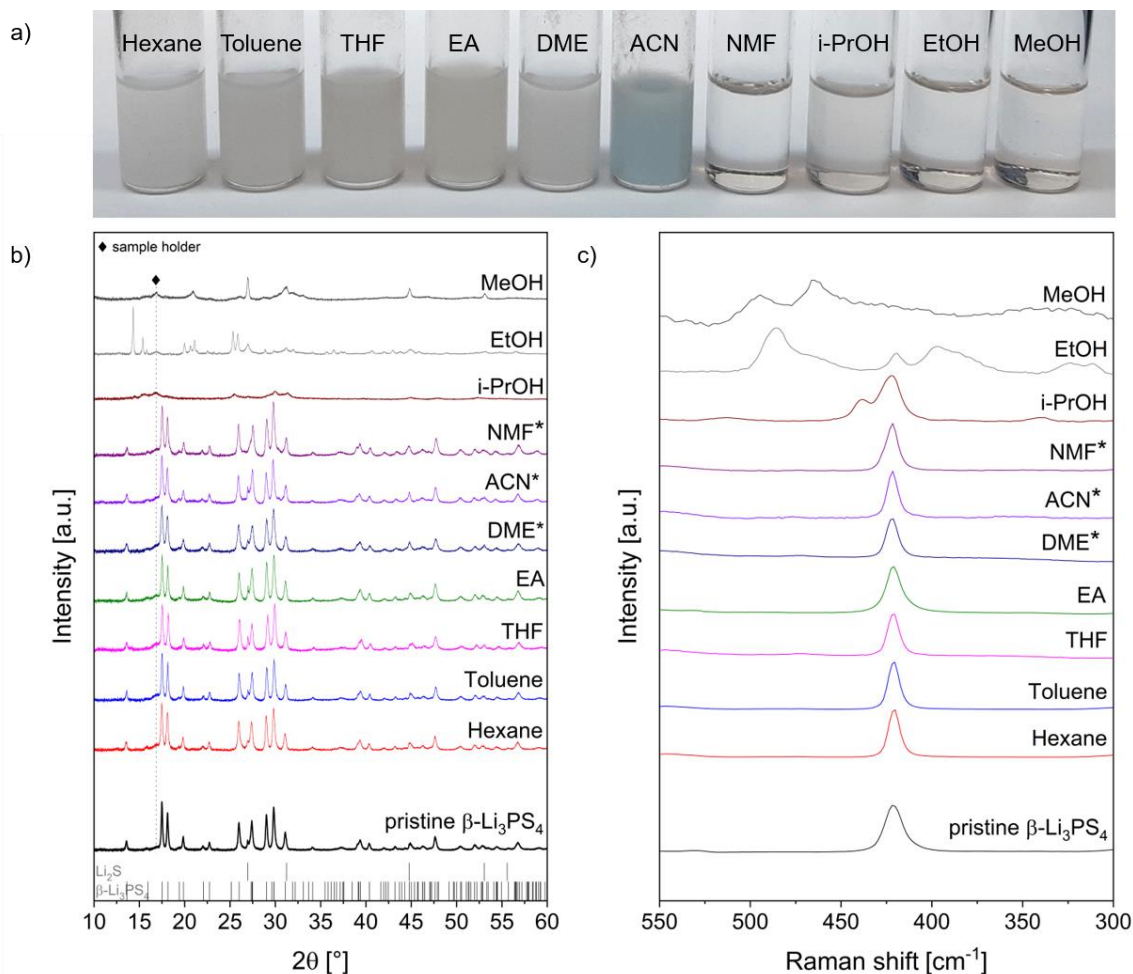


Figure 1: a) Photograph of β - Li_3PS_4 in different organic solvents; b) and c) X-ray diffraction patterns and Raman spectra of dried precipitates obtained after solvent treatment of β - Li_3PS_4 in organic solvents in comparison to pristine β - Li_3PS_4 . To remove the solvents, the samples were heated to 120 °C for 4 h at reduced pressures. To decompose Li_3PS_4 solvent complexes (Figure S1), samples marked with * were additionally heated to 240 °C for 4 h at reduced pressures.

3.2 Dissolution of β - Li_3PS_4 in NMF and its recrystallization mechanism

A complete dissolution of β - Li_3PS_4 in NMF is already observed when using a molar ratio of $\sim 1:14$ of β - Li_3PS_4 to NMF which corresponds to an approximate solid to liquid ratio of 200 mg per 1 ml. For this highest concentration, the obtained clear solution (Figure S2) has a bright yellow color and is highly viscous. Lower relative amounts of NMF cannot fully dissolve β - Li_3PS_4 and a cloudy suspension is formed. An increase of the amount of NMF by a factor of ~ 4 leads, on the other hand, to a significant decrease of the viscosity of the obtained solution. With this, the time needed for the dissolution also drops considerably from ~ 2 h to 2 to 3 min. This lower viscosity is important when considering that in a recycling process a separation of the electrode materials from the electrolyte solution should be performed using filtration or centrifugation.

The boiling point of NMF has been reported to be between 180 and 200 °C.^{43, 44} As described in section 3.1, when using a lower evaporation temperature of 120 °C, the removal of excess NMF from the solution results in the formation of a white powder with an X-ray powder diffraction pattern significantly different to β -Li₃PS₄ (Figure 2 a) for which the crystal structure has not been reported previously. This phase can, however, be transformed into β -Li₃PS₄ after additional heat treatments. For this, the sample was heated to various temperatures between 140 and 240 °C (Figure 2 a). A quantitative phase analysis (Figure 2 b) reveals that temperatures significantly above the boiling point of NMF are required to recrystallize a considerable fraction of β -Li₃PS₄, suggesting that a certain driving force is required to transform the intermediate phase to β -Li₃PS₄. Therefore, it can be assumed that this intermediate phase is a Li₃PS₄·xNMF complex phase as also observed when using other solvents like for example ACN¹² or DME⁵. Only after heating to 240 °C, phase-pure samples are obtained, whereas for all other temperatures phase mixtures of the unknown phase and β -Li₃PS₄ are found. When comparing the XRD patterns of the pristine and the recrystallized β -Li₃PS₄, no significant differences in reflex intensity ratios are found. Rietveld analysis indicates a small change of lattice parameters for the pristine and recrystallized β -Li₃PS₄ ($a_{\text{pristine}} = 12.9959(4)$ Å, $b_{\text{pristine}} = 8.0504(3)$ Å, $c_{\text{pristine}} = 6.1430(2)$ Å vs. $a_{\text{recrystallized}} = 12.9564(5)$ Å, $b_{\text{recrystallized}} = 8.0961(3)$ Å, $c_{\text{recrystallized}} = 6.1428(2)$ Å). The cell volume of the recrystallized β -Li₃PS₄ is bigger by only 0.26 %, suggesting only minimal structural changes (e.g. difference in defect concentrations). Additionally, an increase of the amorphous phase fraction from ~ 8 wt.% in the pristine sample to ~ 35 wt.% in the recrystallized sample was determined using the internal standard method (Figure S3), indicating that the heating temperature of 240 °C is not high enough and/or the duration of 4 h not long enough to obtain a complete recrystallization.

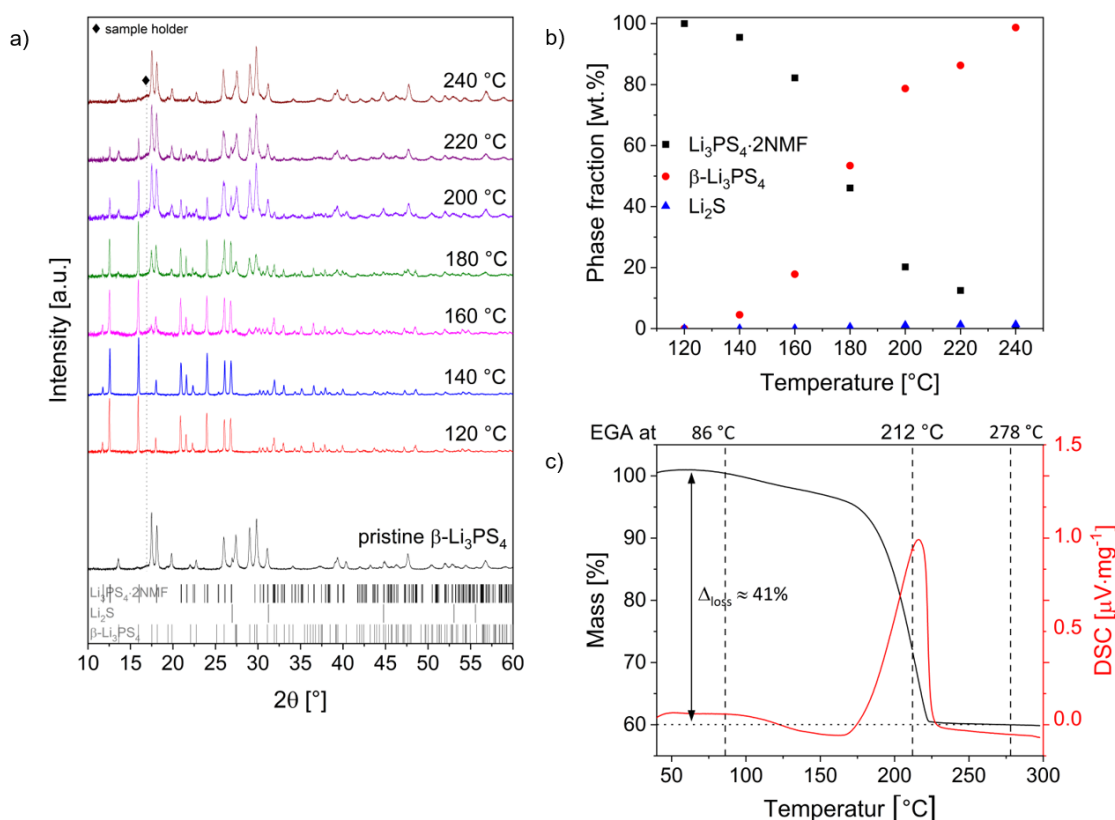


Figure 2: X-ray diffraction patterns (a) and quantitative phase analysis (b) of re-heated samples in comparison to pristine β - Li_3PS_4 and $\text{Li}_3\text{PS}_4 \cdot 2\text{NMF}$ obtained after solvent removal at 120 °C after the treatment of β - Li_3PS_4 in NMF. The samples were heated to temperatures between 140 and 200 °C for 4 h at reduced pressures. c) TG analysis of $\text{Li}_3\text{PS}_4 \cdot 2\text{NMF}$. EG analysis was performed at 86, 212 and 278 °C to investigate which gases are released during the TG analysis. These results are given in Figure S4.

To understand the changes observed upon recrystallization of β - Li_3PS_4 from the intermediate phase and the overall recrystallization mechanism better, the intermediate phase was investigated in more detail and its crystal structure was determined. Indexing of the XRD pattern (Figure 3 a) indicated the formation of a C-centered monoclinic phase with lattice parameters of $a \approx 15.89 \text{ \AA}$, $b \approx 6.02 \text{ \AA}$, $c \approx 16.95 \text{ \AA}$ and $\beta \approx 117.75^\circ$. A weight loss of $\sim 41\%$ in TG analysis (Figure 2 c) shows further that this phase contains approximately 2 NMF molecules per Li_3PS_4 unit suggesting the formation of a complex with composition $\text{Li}_3\text{PS}_4 \cdot 2\text{NMF}$. Evolving gas analysis (Figure S4) confirms that the mass loss is due to the release of NMF from the crystal structure. Moreover, taking space requirements of Li_3PS_4 ^{45, 46} and NMF^{44, 47} into consideration, it can be concluded that the cell is likely to contain 4 formula units per unit cell.

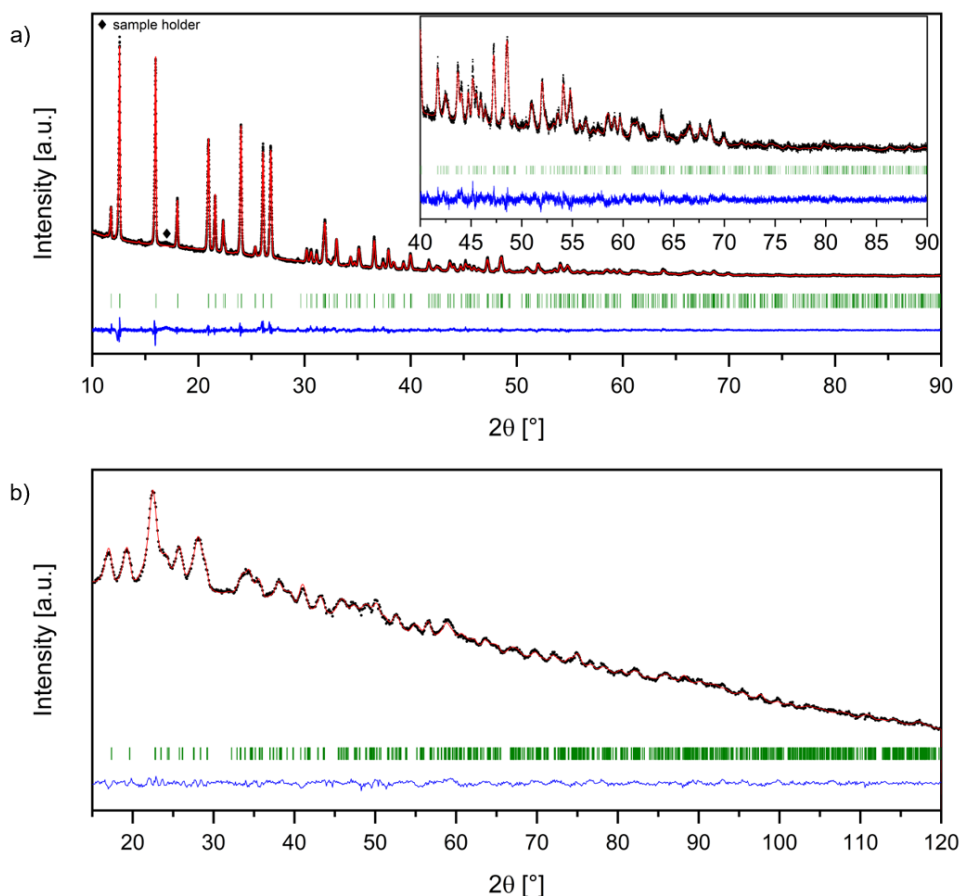


Figure 3: Rietveld refinements of X-ray (a) and neutron (b) diffraction data of $\text{Li}_3\text{PS}_4 \cdot 2\text{NMF}$ with the model obtained using the rigid body method and simulated annealing. The inset in a) shows a magnification of the angular range between 40 and 90°. The comparably low signal-to-noise ratio of the neutron diffraction data is due to incoherent scattering of the hydrogen atoms.

Ab initio structural solution was attempted using the rigid body method in combination with simulated annealing within different *C*-centered monoclinic structures (e.g. *C2/m* and *C2/c*). For this, rigid bodies of PS_4 units (as also indicated from Raman spectroscopy) as well as molecular NMF units were defined based on reported bond lengths and bond angles.⁴⁴⁻⁴⁷ Reasonable flexibility in these parameters was given. Translation, rotation and torsion angles were refined to identify the relative orientations of the different building units. Structural solutions in *C2/m* do not result in a reasonable relative orientation of PS_4 units with sufficient quality of the fits. In contrast, structural solutions in *C2/c* resulted in a plausible orientation of PS_4 and NMF units towards each other, in agreement with the observed systematic extinctions.

By coupling additional neutron diffraction data (Figure 3b), plausible approximate positions of the Li ions could be identified, which are located on two different crystallographic sites (4e and 8f). The corresponding structural parameters after refining the positional and thermal parameters within a Rietveld analysis are given in Table 1. The obtained high thermal parameters of the H ions of the methyl group (H3-H5) indicate a partial disorder in that region

of the structure, most likely explained by the rotational degree of freedom of the methyl group. The crystal structure is represented in Figure 4.

Table 1: Structural parameters of $\text{Li}_3\text{PS}_4 \cdot 2\text{NMF}$ (space group: $C2/c$) as obtained from Rietveld analysis using the rigid body method and simulated annealing.

Atom	Wyckoff position	x	y	z	Occupancy	B [\AA^2]	
Li1	4e	0	0.339(3)	3/4	1	4.0(5)	
Li2	8f	0.820(1)	0.196(3)	0.059(1)	1	9.4(6)	
P1	4e	0	0.8516(6)	3/4	1	3.1(1)	
S1	8f	0.8801(2)	0.0472(3)	0.7083(2)	1	3.1(1)	
S2	8f	0.0137(2)	0.6457(3)	0.8528(1)	1	3.8(1)	
C1	8f	0.6128(5)	0.747(1)	0.0228(4)	1	4.8(1)	
C2	8f	0.691(4)	0.422(5)	0.105(2)	1	4.8(1)	
H1	8f	0.704(8)	0.328(8)	0.160(3)	1	4.7(3)	
H2	8f	0.619(2)	0.620(3)	0.136(3)	1	4.7(3)	
H3	8f	0.663(5)	0.72(1)	0.006(5)	1	20.4(8)	
H4	8f	0.619(7)	0.899(6)	0.045(2)	1	20.4(8)	
H5	8f	0.556(4)	0.734(9)	0.965(3)	1	20.4(8)	
N1	8f	0.634(2)	0.598(3)	0.095(1)	1	4.8(1)	
O1	8f	0.722(4)	0.368(7)	0.055(2)	1	4.8(1)	
<hr/>							
a [\AA]	15.8943(4)	b [\AA]	6.0274(2)	c [\AA]	16.9540(4)	β [$^\circ$]	117.747(2)
R _{wp} (XRD+NPD) [%]	1.26	GOF(XRD+NPD)	1.09	R _{Bragg} [%]	1.69 (XRD)		0.25 (NPD)

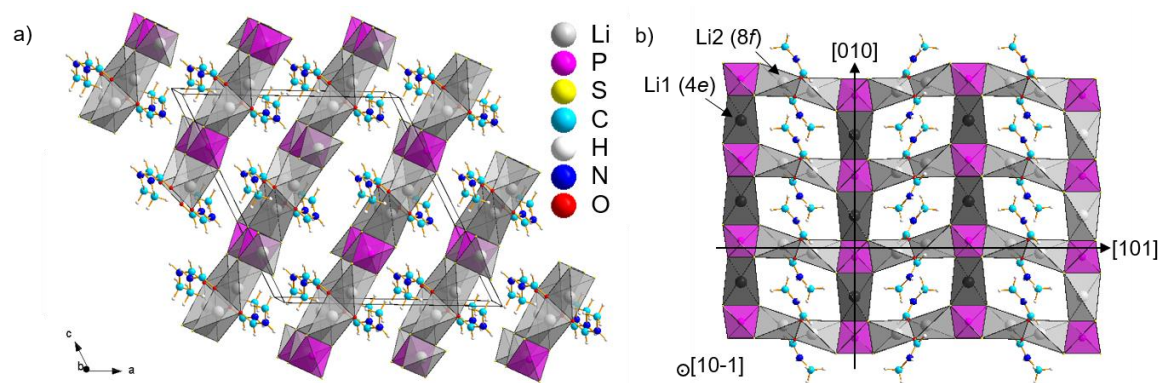


Figure 4: Crystal structure of $\text{Li}_3\text{PS}_4 \cdot 2\text{NMF}$ (a) and top view onto one of the $\text{Li}_3\text{PS}_4 \cdot 2\text{NMF}$ layers (b) as obtained from Rietveld analysis using the rigid body method and simulated annealing.

Additional ab initio DFT simulations confirm the validity of the determined structure. The DFT-optimized structural parameters are given Table S2 for comparison. Most interestingly, they confirm the orientation of the methyl group as well as positioning of the Li2 atom towards the oxygen group of the NMF molecule.

The structure consists of shifted layers of composition $\text{Li}_3\text{PS}_4 \cdot 2\text{NMF}$ stacked along the $[10-1]$ direction. Two different interactions of the molecular species and Li_3PS_4 can be identified: The

oxygen ions are coordinated to the Li ions on the 8f site and the NH groups have a weak interaction with the nearest PS₄ units in the adjacent layers. This results in strong ionic interactions within the layers and weaker dipole interactions perpendicular to them. The latter interaction is also reflected in a change of the NH stretching vibration IR mode (Figure 5 c). This is also important considering the solution mechanism and confirms the role of the NH bonds for stabilizing the PS₄³⁻ units in solution.

Since the Li ions on the 8f site are connected to both PS₄ tetrahedra and NMF molecules, this results in chains according to ...S₂LiO₂LiS₂PS₂LiO₂LiS₂... along the [101] direction. The Li ion on the 4e site is located in a tetrahedral LiS₄ polyhedron between two PS₄ tetrahedra. This results in chains according to ...S₂LiS₂PS₂LiS₂... along the b direction. This interconnectivity of tetrahedra is also highlighted in Figure 4 b).

It becomes also evident that potential interstitial sites within and between Li₃PS₄·2NMF layers are in close distance to the non-polar methyl groups of the NMF molecules. Therefore, their occupation by ionic species such as Li⁺ becomes less likely due to mainly non-ionic weak van-der-Waals forces around them.

When comparing the structure of Li₃PS₄·2NMF to Li₃PS₄·DME⁵ and Li₃PS₄·ACN¹², significant differences can be found. The latter two compounds crystallize in the tetragonal crystal system and consist of alternating layers of Li₂PS₄⁻ separated by layers with composition of (solv)_nLi⁺. In contrast to Li₃PS₄·2NMF, these two structures are more similar to the structure of β-Li₃PS₄ also consisting of Li₂PS₄⁻ layers separated by Li⁺ layers. As the structural transition to the complex can be considered as a topotactic solvent insertion under volume increase, a complete dissolution of β-Li₃PS₄ in DME or ACN is not possible.

Morphological and structural changes of these samples were additionally investigated using a combination of scanning electron microscopy and Raman, infrared as well as X-ray photoelectron spectroscopy (Figure 5 and Figure 6). The morphologies of pristine β-Li₃PS₄ and Li₃PS₄·2NMF are similar with respect to the particle size, however, the particle shapes differ. Li₃PS₄·2NMF particles appear to be less regularly shaped and flakier compared to β-Li₃PS₄. This agrees with the weak dipolar interactions between the layers of Li₃PS₄·2NMF (Figure 4), leading to a comparatively easy peeling off of layers. Recrystallized β-Li₃PS₄ consists of particles with a wider particle size distribution with overall smaller particles. This is probably related to the outgassing of NMF in a random fashion from the crystal structure, resulting in stress fractions of the particles and the formation of grain boundaries.

A comparison between the Raman and FTIR spectra of pristine β-Li₃PS₄, Li₃PS₄·2NMF and recrystallized pristine β-Li₃PS₄ gives further insights into structural changes. Raman spectroscopy (Figure 5 b) confirms that all samples contain ortho-thiophosphate units indicated

by the signal at $\sim 421 \text{ cm}^{-1}$ ^{41, 42}. Other thiophosphate species cannot be observed, neither during the dissolution process (Figure S5 a), nor in $\text{Li}_3\text{PS}_4 \cdot 2\text{NMF}$ or the recrystallized $\beta\text{-Li}_3\text{PS}_4$ after the removal of NMF. The PS_4^{3-} units are also preserved in solution. For $\text{Li}_3\text{PS}_4 \cdot 2\text{NMF}$, less pronounced signals are additionally found at ~ 315 and 388 cm^{-1} which can be assigned to the NMF within the structure. ⁹ The most significant differences in the FTIR spectra (Figure 5 c) can be again ascribed to the presence of NMF in the samples. A comparison of the spectra of pure NMF, $\beta\text{-Li}_3\text{PS}_4$ dissolved in NMF and $\text{Li}_3\text{PS}_4 \cdot 2\text{NMF}$ (Figure S5 a) reveals characteristic shifts of NMF vibration modes which dominate the spectra as the pristine $\beta\text{-Li}_3\text{PS}_4$ features no strong signals. As already mentioned, the strongest shift is observed for the NH stretching vibration mode in the range between 3100 and 3480 cm^{-1} which can be attributed to the interactions between NH groups of NMF molecules and PS_4^{3-} units in the layered structure of $\text{Li}_3\text{PS}_4 \cdot 2\text{NMF}$.⁴⁸ Other modes (e.g. the CH_3 symmetric bend at $\sim 1375 \text{ cm}^{-1}$) show less pronounced shifts since weaker interactions take place. Similar trends in band shifting are observed in the Raman spectra. The NMF related signals in the FTIR spectra of the recrystallized $\beta\text{-Li}_3\text{PS}_4$ decrease significantly, however, there seems to be still a smaller fraction of NMF present in the sample. It is unlikely that these traces remain in the crystal structure of the recrystallized sample as its presence is not indicated with respect to the cell volume of the crystalline phase formed. Additionally, the TG and EG analysis shows that NMF is released at temperatures $< 240 \text{ }^\circ\text{C}$ used for drying of the recrystallized sample. NMF might, however, be present as surface adsorbates or in amorphous phases. In addition, the spectra of pristine and recrystallized $\beta\text{-Li}_3\text{PS}_4$ feature two signals at ~ 1042 and 961 cm^{-1} , which could indicate the formation of small amounts of $\text{PS}_{4-x}\text{O}_x^{3-}$ groups.⁴⁹ However, there is no indication for such $\text{PS}_{4-x}\text{O}_x^{3-}$ species in Raman spectroscopy ^{50, 51} and XRD (at least not in the form of crystalline phases). This also illustrates that special attention has to be paid to the amorphous phase fraction present in the sample since subtle changes in the composition of the amorphous phase (i.e., formation of phases other than amorphous Li_3PS_4) could have a significant influence on the properties of the recrystallized phases.

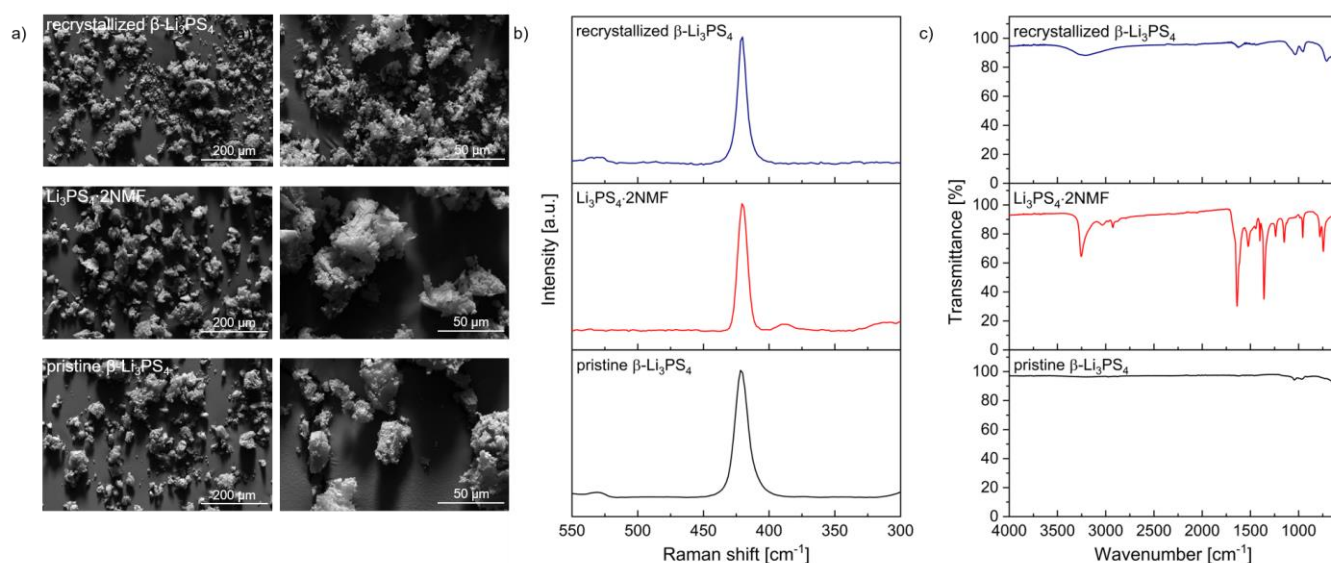


Figure 5: Comparison of scanning electron micrographs (a), Raman (b) and FTIR (c) spectra of pristine β - Li_3PS_4 , $\text{Li}_3\text{PS}_4 \cdot 2\text{NMF}$ and recrystallized β - Li_3PS_4 .

Since the XRD analysis and Raman and FTIR spectroscopy do not show considerable structural changes between pristine and recrystallized β - Li_3PS_4 , XPS measurements were additionally carried out. The comparison between the $\text{P}2p$ and $\text{S}2p$ spectra of the pristine and recrystallized β - Li_3PS_4 are shown in Figure 6. The main signal corresponds to the P-S bond in the PS_4^{3-} units of β - Li_3PS_4 at 132.0 eV ($\text{P}2p$) and 161.7 eV ($\text{S}2p$).⁵²⁻⁵⁴ The low-intensity signals at lower binding energies than the PS_4^{3-} peaks can be assigned to reduced phosphorous species Li_xP ($0 < x < 3$) and Li_2S in the $\text{P}2p$ and $\text{S}2p$ spectra, respectively.^{53, 55} The latter agrees with the Li_2S impurity phase observed in the XRD measurements. The presence of P-[S]_n-P type bonds is indicated from the doublet at ~ 163.0 and 164.2 eV in the $\text{S}2p$ spectrum.⁵⁵ An unambiguous assignment of the signal found at higher binding energies in the $\text{P}2p$ spectrum is not possible since P-[S]_n-P as well as oxygenated phosphorous species (phosphates, metaphosphates or $\text{PS}_{4-x}\text{O}_x^{3-}$)^{32, 56} can be present at these binding energies impeding the deconvolution. For the recrystallized β - Li_3PS_4 , a small shift to higher energies as well as a small increase in concentration of this signal is found. This indicates that oxygenated phosphorous species, possessing higher binding energies than P-[S]_n-P^{57, 58}, might have formed to a minor extent in addition to P-[S]_n-P. Most likely, these species can be assigned to the amorphous phase fraction since additional reflections are absent in the diffraction data. Besides this, an increase in the intensity of carbonate-related signals in the $\text{C}1s$ and $\text{O}1s$ spectra is observed in the recrystallized sample compared to the pristine sample. Nevertheless, no significant changes are observed suggesting minor degradation of the recrystallized β - Li_3PS_4 in comparison to the pristine β - Li_3PS_4 after the solvent treatment.

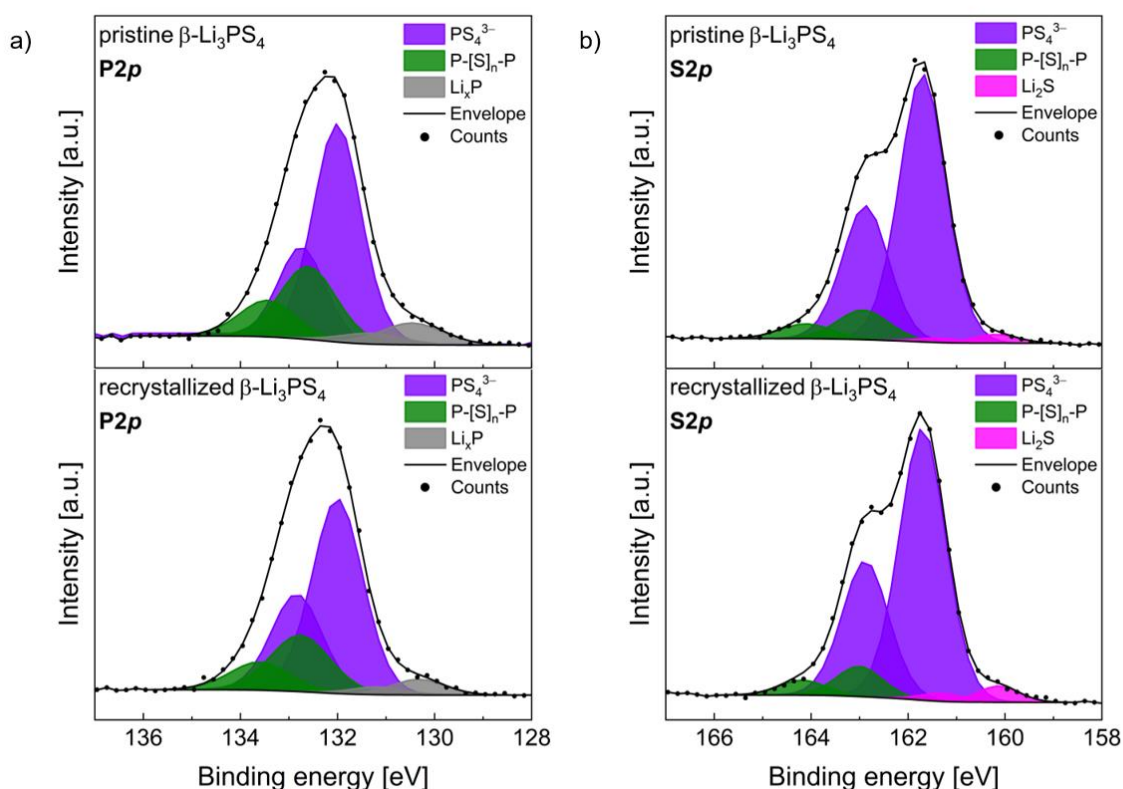


Figure 6: Comparison between P2p (a) and S2p (b) XPS spectra of pristine and recrystallized β -Li₃PS₄.

To investigate the influence of the solvent treatment on the ionic conductivity, impedance measurements were performed on pristine β -Li₃PS₄, Li₃PS₄·2NMF and recrystallized β -Li₃PS₄. The Nyquist plot of the pristine and recrystallized β -Li₃PS₄ (measured at 25 °C) is shown in Figure 7 a). Both samples show at first glance a similar behavior with a half semi-circle and an x-axis intercept at high frequencies and a mid- and low-frequency tail. The Bode plots (Figure S6) indicate that a single Li-conducting phenomenon is dominant. It was found that a single, parallel R/CPE element (R=resistor, CPE=constant phase element) connected in series to a CPE can be used for fitting the Li-ion transport process and electrode-ion-blocking effect at the electrode, respectively. From the fits, the conductivity values of pristine and recrystallized β -Li₃PS₄ were determined to be $2.34 \cdot 10^{-5} \text{ S} \cdot \text{cm}^{-1}$ and $2.18 \cdot 10^{-5} \text{ S} \cdot \text{cm}^{-1}$ at 25 °C, respectively, which is the same within experimental error.⁵⁹ The capacitance values for the pristine and recrystallized β -Li₃PS₄ are with $3 \cdot 10^{-11} \text{ F}$ vs. $8 \cdot 10^{-11} \text{ F}$, respectively, slightly different, though in the same order of magnitude. Remarkably, the activation energies of both samples are with 0.38 and 0.20 eV significantly different (Figure 7 c). The lower activation energy of recrystallized β -Li₃PS₄ could be assigned to a higher amount of amorphous phase fraction in the recrystallized phase, which was reported to be beneficial for the bulk transport of Li⁺ ions.⁶⁰ On the other hand, the higher capacitance observed for the recrystallized sample also indicates an increased influence of grain boundaries, which might be related to slightly different surface properties (e.g., induced by solvent residuals) and chemical species being present after the

recrystallization process. The asymmetry observed in the Bode plot of the recrystallized sample (Figure S6) likely indicates a more complex conduction behavior beyond a single transport process. However, due to similar time constants, these processes cannot be well deconvoluted from each other.

On the contrary, $\text{Li}_3\text{PS}_4 \cdot 2\text{NMF}$ shows a completely different response. From the Nyquist plot (Figure 7 b), only a single semicircle could be observed within the high and mid frequency range along with a low frequency intercept on the x-axis and no blocking tail, which indicates that this phase is considerably less Li-ion conducting with an insufficient conductivity for an application within a solid-state battery. This can further be confirmed from the Bode plots (Figure S6), where at low frequencies the phase angle is found to be closer 0° , indicating a resistive instead of a capacitive behavior. To obtain a good estimate of the overall resistance, two R/CPE elements were used in series. From this, a conductivity value of $1.66 \cdot 10^{-9} \text{ S} \cdot \text{cm}^{-1}$ at 25°C was calculated, which is 4 orders of magnitude lower than that of the pristine and the recrystallized $\beta\text{-Li}_3\text{PS}_4$. This decreased ion conductivity is expected with respect to the crystal structure of $\text{Li}_3\text{PS}_4 \cdot 2\text{NMF}$ since there are no continuous pathways for Li-ion conduction, and due to strong ionic interactions between lithium ions and the oxygen ions of the solvent molecules. The significantly higher activation barrier of 0.70 eV (Figure 7 c) is again in agreement with the absence of additional interstitial lithium sites within the compound. It can be deduced that any remaining crystalline $\text{Li}_3\text{PS}_4 \cdot 2\text{NMF}$ would have a detrimental impact on the conductivity of recrystallized samples after a solvent treatment in a possible recycling application. Therefore, it is essential to optimize the solvent removal procedure in order to avoid highly resistive residuals which would lead to a reduced electrolyte performance. At the same time, it might be beneficial to find a compromise between the formation of recrystallized and amorphous phases fractions in order to obtain optimized conductivities.

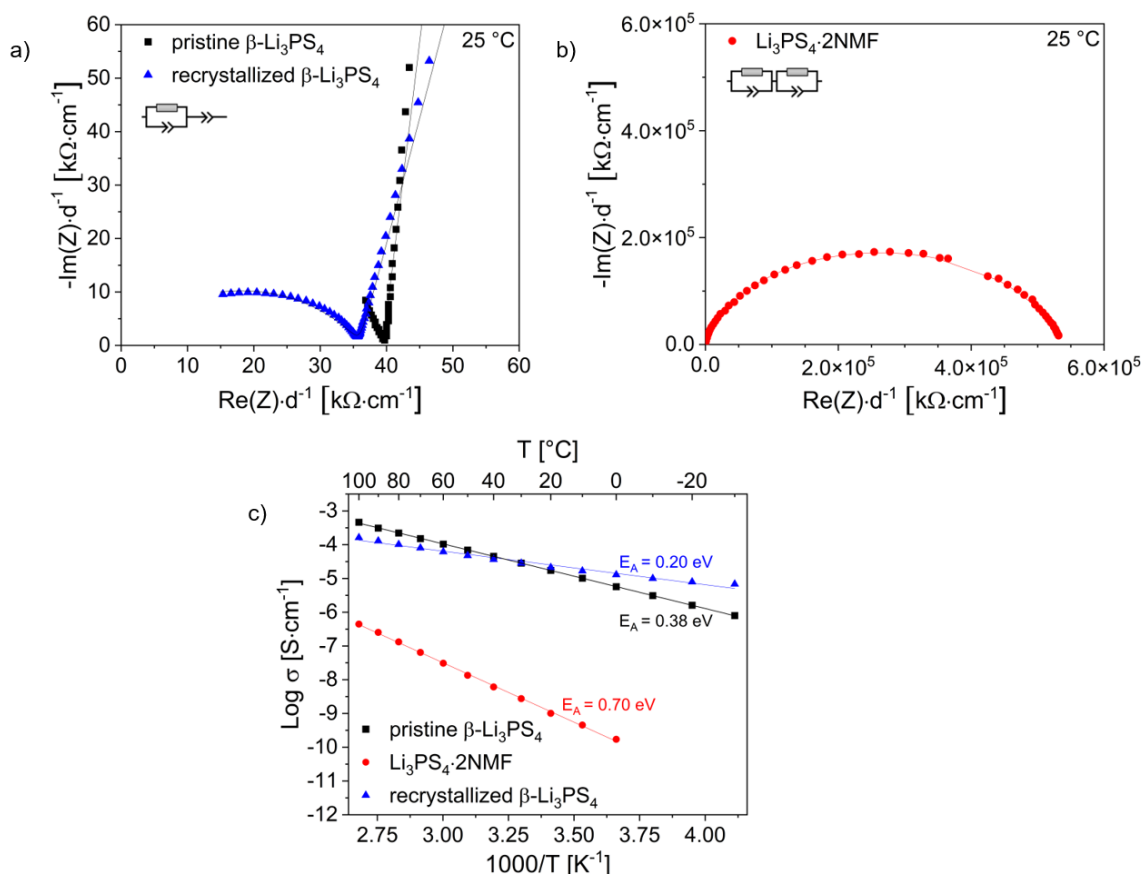


Figure 7: Nyquist plots of pristine and recrystallized $\beta\text{-Li}_3\text{PS}_4$ (a) and $\text{Li}_3\text{PS}_4 \cdot 2\text{NMF}$ (b) measured at 25 °C with corresponding fits and Arrhenius plots (c).

4 Conclusions

The study shown here highlights the importance of separating solvent-based synthesis from dissolution and recrystallization strategies of $\beta\text{-Li}_3\text{PS}_4$. Though many solvents have been reported to be suitable for the synthesis of $\beta\text{-Li}_3\text{PS}_4$, recrystallization requires the use of polar, weakly protic solvents such as NMF. The recrystallization proceeds via the intermediate phase $\text{Li}_3\text{PS}_4 \cdot 2\text{NMF}$, which needs to be fully removed using an optimized heating process. This step is necessary in order to obtain conductivities of the recrystallized $\beta\text{-Li}_3\text{PS}_4$ comparable to the pristine material.

We emphasize that the increase in amorphous phase has to be regarded as critical for the use of a recrystallization procedure within a recycling process. Though it leads to comparable room temperature conductivities, it is so far not clear to what extent repeated dissolution and recrystallization might impact the functional electrolyte properties which will be decisive to establish these materials within a circular economy. Furthermore, the role of the electrode materials within the electrode composites needs to be considered which might demonstrate the necessity to adapt the recrystallization to the electrode materials used. This will be reported in a follow-up article.

5 Acknowledgements

This work has been funded by German federal state of Hessen (Hessen Agentur, HA-Project Number 848/20-08). LMR. and JJ. acknowledge the financial support by the German Federal Ministry of Research and Education (BMBF), projects 03XP0433D and 03XP0430A (FestBatt). CS and BVL acknowledge financial support by the German Federal Ministry of Research and Education (BMBF), projects 03XP0177B (FestBatt) and the Deutsche Forschungsgemeinschaft via the Cluster of Excellence e-conversion (EXC2089). YI and BG acknowledge the funding from the European Research Council (ERC) under the European Union's Horizon 2020 research and innovation programme (grant agreement No. 865855), the support by the Stuttgart Center for Simulation Science (SimTech), and the support by the state of Baden-Württemberg through bwHPC and the German Research Foundation (DFG) through grant no INST 40/467-1 FUGG (JUSTUS cluster).

6 Authors' Contribution

KW, WE and OC conceived and designed the study. KW prepared the samples, measured and analyzed the XRD, SEM, Raman and FTIR spectroscopy data. LR measured and analyzed the XPS data. KW and LMR performed the EIS, and interpreted the data together with AIW under the guidance of JJ. TF measured neutron diffraction. CS measured and analyzed TGA and EGA under the guidance of BVL. YI performed the DFT calculations under the guidance of BG. RED helped with the analysis of diffraction data. KW wrote the manuscript. All authors discussed and revised the work.

7 Conflicts of Interest

There are no conflicts of interest to declare.

8 References

1. Zhang, Q.; Cao, D.; Ma, Y.; Natan, A.; Aurora, P.; Zhu, H., Sulfide-Based Solid-State Electrolytes: Synthesis, Stability, and Potential for All-Solid-State Batteries. **2019**, *31* (44), 1901131.
2. Wang, H.; Hood, Z. D.; Xia, Y.; Liang, C., Fabrication of ultrathin solid electrolyte membranes of β -Li₃PS₄ nanoflakes by evaporation-induced self-assembly for all-solid-state batteries. *Journal of Materials Chemistry A* **2016**, *4* (21), 8091-8096.
3. Lim, H.-D.; Lim, H.-K.; Xing, X.; Lee, B.-S.; Liu, H.; Coaty, C.; Kim, H.; Liu, P., Solid Electrolyte Layers by Solution Deposition. *Advanced Materials Interfaces* **2018**, *5* (8), 1701328.
4. Phuc, N. H. H.; Morikawa, K.; Totani, M.; Muto, H.; Matsuda, A., Chemical synthesis of Li₃PS₄ precursor suspension by liquid-phase shaking. *Solid State Ionics* **2016**, *285*, 2-5.
5. Sedlmaier, S. J.; Indris, S.; Dietrich, C.; Yavuz, M.; Dräger, C.; von Seggern, F.; Sommer, H.; Janek, J., Li₄PS₄: A Li⁺ Superionic Conductor Synthesized by a Solvent-Based Soft Chemistry Approach. *Chem. Mater.* **2017**, *29* (4), 1830-1835.

6. Phuc, N. H. H.; Totani, M.; Morikawa, K.; Muto, H.; Matsuda, A., Preparation of Li_3PS_4 solid electrolyte using ethyl acetate as synthetic medium. *Solid State Ionics* **2016**, *288*, 240-243.
7. Ito, A.; Kimura, T.; Sakuda, A.; Tatsumisago, M.; Hayashi, A., Liquid-phase synthesis of Li_3PS_4 solid electrolyte using ethylenediamine. *J. Sol-Gel Sci. Technol.* **2022**, *101* (1), 2-7.
8. Teragawa, S.; Aso, K.; Tadanaga, K.; Hayashi, A.; Tatsumisago, M., Liquid-phase synthesis of a Li_3PS_4 solid electrolyte using N-methylformamide for all-solid-state lithium batteries. *Journal of Materials Chemistry A* **2014**, *2* (14), 5095-5099.
9. Teragawa, S.; Aso, K.; Tadanaga, K.; Hayashi, A.; Tatsumisago, M., Formation of $\text{Li}_2\text{S-P}_2\text{S}_5$ Solid Electrolyte from N-Methylformamide Solution. *Chem. Lett.* **2013**, *42* (11), 1435-1437.
10. Teragawa, S.; Aso, K.; Tadanaga, K.; Hayashi, A.; Tatsumisago, M., Preparation of $\text{Li}_2\text{S-P}_2\text{S}_5$ solid electrolyte from N-methylformamide solution and application for all-solid-state lithium battery. *J. Power Sources* **2014**, *248*, 939-942.
11. Liu, Z.; Fu, W.; Payzant, E. A.; Yu, X.; Wu, Z.; Dudney, N. J.; Kiggans, J.; Hong, K.; Rondinone, A. J.; Liang, C., Anomalous High Ionic Conductivity of Nanoporous $\beta\text{-Li}_3\text{PS}_4$. *Journal of the American Chemical Society* **2013**, *135* (3), 975-978.
12. Calpa, M.; Nakajima, H.; Mori, S.; Goto, Y.; Mizuguchi, Y.; Moriyoshi, C.; Kuroiwa, Y.; Rosero-Navarro, N. C.; Miura, A.; Tadanaga, K., Formation Mechanism of $\beta\text{-Li}_3\text{PS}_4$ through Decomposition of Complexes. *Inorg. Chem.* **2021**, *60* (10), 6964-6970.
13. Azhari, L.; Bong, S.; Ma, X.; Wang, Y., Recycling for All Solid-State Lithium-Ion Batteries. *Matter* **2020**, *3* (6), 1845-1861.
14. Tan, D. H. S.; Xu, P.; Yang, H.; Kim, M.-c.; Nguyen, H.; Wu, E. A.; Doux, J.-M.; Banerjee, A.; Meng, Y. S.; Chen, Z., Sustainable design of fully recyclable all solid-state batteries. *MRS Energy & Sustainability* **2020**, *7*, E23.
15. Hatz, A.-K.; Calaminus, R.; Feijoo, J.; Treber, F.; Blahusch, J.; Lenz, T.; Reichel, M.; Karaghiosoff, K.; Vargas-Barbosa, N. M.; Lotsch, B. V., Chemical Stability and Ionic Conductivity of LGPS-Type Solid Electrolyte Tetra- Li_7SiPS_8 after Solvent Treatment. *ACS Applied Energy Materials* **2021**, *4* (9), 9932-9943.
16. Nam, Y. J.; Cho, S.-J.; Oh, D. Y.; Lim, J.-M.; Kim, S. Y.; Song, J. H.; Lee, Y.-G.; Lee, S.-Y.; Jung, Y. S., Bendable and Thin Sulfide Solid Electrolyte Film: A New Electrolyte Opportunity for Free-Standing and Stackable High-Energy All-Solid-State Lithium-Ion Batteries. *Nano Lett.* **2015**, *15* (5), 3317-3323.
17. Lee, K.; Kim, S.; Park, J.; Park, S. H.; Coskun, A.; Jung, D. S.; Cho, W.; Choi, J. W., Selection of Binder and Solvent for Solution-Processed All-Solid-State Battery. *J. Electrochem. Soc.* **2017**, *164* (9), A2075-A2081.
18. Sakuda, A.; Kuratani, K.; Yamamoto, M.; Takahashi, M.; Takeuchi, T.; Kobayashi, H., All-Solid-State Battery Electrode Sheets Prepared by a Slurry Coating Process. *J. Electrochem. Soc.* **2017**, *164* (12), A2474-A2478.
19. Yamamoto, M.; Terauchi, Y.; Sakuda, A.; Takahashi, M., Slurry mixing for fabricating silicon-composite electrodes in all-solid-state batteries with high areal capacity and cycling stability. *J. Power Sources* **2018**, *402*, 506-512.
20. Yamamoto, M.; Terauchi, Y.; Sakuda, A.; Takahashi, M., Binder-free sheet-type all-solid-state batteries with enhanced rate capabilities and high energy densities. *Scientific Reports* **2018**, *8* (1), 1212.
21. Yamamoto, M.; Takahashi, M.; Terauchi, Y.; Kobayashi, Y.; Ikeda, S.; Sakuda, A., Fabrication of composite positive electrode sheet with high active material content and effect of fabrication pressure for all-solid-state battery. *J. Ceram. Soc. Jpn.* **2017**, *125* (5), 391-395.
22. Ito, S.; Fujiki, S.; Yamada, T.; Aihara, Y.; Park, Y.; Kim, T. Y.; Baek, S.-W.; Lee, J.-M.; Doo, S.; Machida, N., A rocking chair type all-solid-state lithium ion battery adopting $\text{Li}_2\text{O-ZrO}_2$ coated $\text{LiNi}_{0.8}\text{Co}_{0.15}\text{Al}_{0.05}\text{O}_2$ and a sulfide based electrolyte. *J. Power Sources* **2014**, *248*, 943-950.
23. Hood, Z. D.; Wang, H.; Pandian, A. S.; Peng, R.; Gilroy, K. D.; Chi, M.; Liang, C.; Xia, Y., Fabrication of Sub-Micrometer-Thick Solid Electrolyte Membranes of $\beta\text{-Li}_3\text{PS}_4$ via Tiled Assembly of Nanoscale, Plate-Like Building Blocks. *Advanced Energy Materials* **2018**, *8* (21), 1800014.

24. Oh, D. Y.; Kim, D. H.; Jung, S. H.; Han, J.-G.; Choi, N.-S.; Jung, Y. S., Single-step wet-chemical fabrication of sheet-type electrodes from solid-electrolyte precursors for all-solid-state lithium-ion batteries. *Journal of Materials Chemistry A* **2017**, *5* (39), 20771-20779.
25. Van Eijck, L.; Cussen, L. D.; Sykora, G. J.; Schooneveld, E. M.; Rhodes, N. J.; Van Well, A. A., Design and Performance of a Novel Neutron Powder Diffractometer: PEARL at TU Delft. *J. Appl. Crystallogr.* **2016**, *49* (5), 1398-1401.
26. Kresse, G.; Furthmüller, J., Efficiency of ab-initio total energy calculations for metals and semiconductors using a plane-wave basis set. *Computational Materials Science* **1996**, *6* (1), 15-50.
27. Kresse, G.; Joubert, D., From ultrasoft pseudopotentials to the projector augmented-wave method. *Physical Review B* **1999**, *59* (3), 1758-1775.
28. Kresse, G.; Furthmüller, J., Efficient iterative schemes for ab initio total-energy calculations using a plane-wave basis set. *Physical Review B* **1996**, *54* (16), 11169-11186.
29. Blöchl, P. E., Projector augmented-wave method. *Phys. Rev. B.* **1994**, *50* (24), 17953-17979.
30. Perdew, J. P.; Burke, K.; Ernzerhof, M., Generalized Gradient Approximation Made Simple. *Phys. Rev. Lett.* **1996**, *77*, 3865.
31. Blöchl, P. E.; Jepsen, O.; Andersen, O. K., Improved tetrahedron method for Brillouin-zone integrations. *Physical Review B* **1994**, *49* (23), 16223-16233.
32. Teo, J. H.; Strauss, F.; Walther, F.; Ma, Y.; Payandeh, S.; Scherer, T.; Bianchini, M.; Janek, J.; Brezesinski, T., The interplay between (electro)chemical and (chemo)mechanical effects in the cycling performance of thiophosphate-based solid-state batteries. *Materials Futures* **2022**, *1* (1), 015102.
33. Walther, F.; Strauss, F.; Wu, X.; Mogwitz, B.; Hertle, J.; Sann, J.; Rohnke, M.; Brezesinski, T.; Janek, J., The Working Principle of a $\text{Li}_2\text{CO}_3/\text{LiNbO}_3$ Coating on NCM for Thiophosphate-Based All-Solid-State Batteries. *Chem. Mater.* **2021**, *33* (6), 2110-2125.
34. Dubois, P.; Lelieur, J.; Lepoutre, G., Identification and characterization of lithium polysulfides in solution in liquid ammonia. *Inorg. Chem.* **1988**, *27* (1), 73-80.
35. Chivers, T., Ubiquitous trisulphur radical ion S_3^- . *Nature* **1974**, *252* (5478), 32-33.
36. Ruhl, J.; Riegger, L. M.; Ghidui, M.; Zeier, W. G., Impact of Solvent Treatment of the Superionic Argyrodite $\text{Li}_6\text{PS}_5\text{Cl}$ on Solid-State Battery Performance. *Advanced Energy and Sustainability Research* **2021**, *2* (2), 2000077.
37. Ziolkowska, D. A.; Arnold, W.; Druffel, T.; Sunkara, M.; Wang, H., Rapid and Economic Synthesis of a Li_7PS_6 Solid Electrolyte from a Liquid Approach. *ACS Applied Materials & Interfaces* **2019**, *11* (6), 6015-6021.
38. Yubuchi, S.; Uematsu, M.; Hotehama, C.; Sakuda, A.; Hayashi, A.; Tatsumisago, M., An argyrodite sulfide-based superionic conductor synthesized by a liquid-phase technique with tetrahydrofuran and ethanol. *Journal of Materials Chemistry A* **2019**, *7* (2), 558-566.
39. Zhou, L.; Park, K.-H.; Sun, X.; Lalère, F.; Adermann, T.; Hartmann, P.; Nazar, L. F., Solvent-Engineered Design of Argyrodite $\text{Li}_6\text{PS}_5\text{X}$ (X = Cl, Br, I) Solid Electrolytes with High Ionic Conductivity. *ACS Energy Letters* **2018**, *4* (1), 265-270.
40. Yubuchi, S.; Uematsu, M.; Deguchi, M.; Hayashi, A.; Tatsumisago, M., Lithium-Ion-Conducting Argyrodite-Type $\text{Li}_6\text{PS}_5\text{X}$ (X = Cl, Br, I) Solid Electrolytes Prepared by a Liquid-Phase Technique Using Ethanol as a Solvent. *ACS Applied Energy Materials* **2018**, *1* (8), 3622-3629.
41. Dietrich, C.; Weber, D. A.; Sedlmaier, S. J.; Indris, S.; Culver, S. P.; Walter, D.; Janek, J.; Zeier, W. G., Lithium ion conductivity in $\text{Li}_2\text{S}-\text{P}_2\text{S}_5$ glasses – building units and local structure evolution during the crystallization of superionic conductors Li_3PS_4 , $\text{Li}_7\text{P}_3\text{S}_{11}$ and $\text{Li}_4\text{P}_2\text{S}_7$. *Journal of Materials Chemistry A* **2017**, *5* (34), 18111-18119.
42. Machida, N.; Yamamoto, H.; Asano, S.; Shigematsu, T., Preparation of amorphous $75\text{Li}_2\text{S} \cdot x\text{P}_2\text{S}_3 \cdot (25-x)\text{P}_2\text{S}_5$ (mol%) solid electrolytes by a high-energy ball-milling process and their application for an all-solid-state lithium battery. *Solid State Ionics* **2005**, *176* (5), 473-479.
43. Appendix A. Properties, Purification, and Use of Organic Solvents. In *Solvents and Solvent Effects in Organic Chemistry*, 2010; pp 549-586.

44. PubChem Compound Summary for CID 31254, N-Methylformamide. <https://pubchem.ncbi.nlm.nih.gov/compound/N-Methylformamide> (accessed August 17, 2022).
45. Mercier, R.; Malugani, J.-P.; Fahys, B.; Robert, G.; Douglade, J., Structure du tetrathio phosphate de lithium. *Acta Crystallographica Section B* **1982**, *38* (7), 1887-1890.
46. Homma, K.; Yonemura, M.; Kobayashi, T.; Nagao, M.; Hirayama, M.; Kanno, R., Crystal structure and phase transitions of the lithium ionic conductor Li₃PS₄. *Solid State Ionics* **2011**, *182* (1), 53-58.
47. Kitano, M.; Kuchitsu, K., Molecular Structure of N-Methylformamide as Studied by Gas Electron Diffraction. *Bull. Chem. Soc. Jpn.* **1974**, *47* (3), 631-634.
48. Isao, S., Infrared Spectra and Normal Vibrations of Thioamides. III. N-Methylthioformamide and N-Methylthioacetamide. *Bull. Chem. Soc. Jpn.* **1962**, *35* (9), 1456-1464.
49. Brockner, W.; Jendrzok, B.; Menzel, F.; Jensen, V. R.; Ystenes, M., Vibrational spectra and ab initio quantum mechanical calculation of energy, geometry and vibrational frequencies of the oxothiophosphate ions PO₃S₃⁻, PO₂S₃⁻² and POS₃⁻³. *J. Mol. Struct.* **1994**, *319*, 85-100.
50. Popović, L.; Manoun, B.; de Waal, D.; Nieuwoudt, M. K.; Comins, J. D., Raman spectroscopic study of phase transitions in Li₃PO₄. *Journal of Raman Spectroscopy* **2003**, *34* (1), 77-83.
51. Matsuda, Y.; Kuwata, N.; Okawa, T.; Dorai, A.; Kamishima, O.; Kawamura, J., In situ Raman spectroscopy of Li_xCoO₂ cathode in Li/Li₃PO₄/LiCoO₂ all-solid-state thin-film lithium battery. *Solid State Ionics* **2019**, *335*, 7-14.
52. Kato, A.; Kowada, H.; Deguchi, M.; Hotehama, C.; Hayashi, A.; Tatsumisago, M., XPS and SEM analysis between Li/Li₃PS₄ interface with Au thin film for all-solid-state lithium batteries. *Solid State Ionics* **2018**, *322*, 1-4.
53. Wenzel, S.; Sedlmaier, S. J.; Dietrich, C.; Zeier, W. G.; Janek, J., Interfacial reactivity and interphase growth of argyrodite solid electrolytes at lithium metal electrodes. *Solid State Ionics* **2018**, *318*, 102-112.
54. Wood, K. N.; Steirer, K. X.; Hafner, S. E.; Ban, C.; Santhanagopalan, S.; Lee, S.-H.; Teeter, G., Operando X-ray photoelectron spectroscopy of solid electrolyte interphase formation and evolution in Li₂S-P₂S₅ solid-state electrolytes. *Nature Communications* **2018**, *9* (1), 2490.
55. Koerver, R.; Walther, F.; Aygün, I.; Sann, J.; Dietrich, C.; Zeier, W. G.; Janek, J., Redox-active cathode interphases in solid-state batteries. *Journal of Materials Chemistry A* **2017**, *5* (43), 22750-22760.
56. Ma, Y.; Teo, J. H.; Walther, F.; Ma, Y.; Zhang, R.; Mazilkin, A.; Tang, Y.; Goonetilleke, D.; Janek, J.; Bianchini, M.; Brezesinski, T., Advanced Nanoparticle Coatings for Stabilizing Layered Ni-Rich Oxide Cathodes in Solid-State Batteries. *Adv. Funct. Mater.* **2022**, *32* (23), 2111829.
57. Wang, B.; Liu, J.; Sun, Q.; Li, R.; Sham, T.-K.; Sun, X., Atomic layer deposition of lithium phosphates as solid-state electrolytes for all-solid-state microbatteries. *Nanotechnology* **2014**, *25* (50), 504007.
58. Appapillai, A. T.; Mansour, A. N.; Cho, J.; Shao-Horn, Y., Microstructure of LiCoO₂ with and without "AlPO₄" Nanoparticle Coating: Combined STEM and XPS Studies. *Chem. Mater.* **2007**, *19* (23), 5748-5757.
59. Ohno, S.; Berges, T.; Buchheim, J.; Duchardt, M.; Hatz, A.-K.; Kraft, M. A.; Kwak, H.; Santhosha, A. L.; Liu, Z.; Minafra, N.; Tsuji, F.; Sakuda, A.; Schlem, R.; Xiong, S.; Zhang, Z.; Adelhelm, P.; Chen, H.; Hayashi, A.; Jung, Y. S.; Lotsch, B. V.; Roling, B.; Vargas-Barbosa, N. M.; Zeier, W. G., How Certain Are the Reported Ionic Conductivities of Thiophosphate-Based Solid Electrolytes? An Interlaboratory Study. *ACS Energy Letters* **2020**, *5* (3), 910-915.
60. Marchini, F.; Porcheron, B.; Rouse, G.; Alberio Blanquer, L.; Droguet, L.; Foix, D.; Koç, T.; Deschamps, M.; Tarascon, J. M., The Hidden Side of Nanoporous β-Li₃PS₄ Solid Electrolyte. *Advanced Energy Materials* **2021**, *11* (34), 2101111.

Supplementary Information for

Dissolution and Recrystallization Behavior of Li_3PS_4 in Different Organic Solvents

Kerstin Wissel^{a,*}, Luise M. Riegger^{b,c}, Christian Schneider^d, Aamir I. Waidha^a, Theodosios Famprakis^e, Yuji Ikeda^f, Blazej Grabowski^f, Robert E. Dinnebier^d, Bettina V. Lotsch^{d,g}, Jürgen Janek^{b,c}, Wolfgang Ensinger^a and Oliver Clemens^h

^a Technical University of Darmstadt, Institute for Materials Science, Materials Analysis, Alarich-Weiss-Straße 2, 64287 Darmstadt, Germany

^b Justus-Liebig-University Gießen, Institute for Physical Chemistry, Heinrich-Buff-Ring 17, 35392 Gießen, Germany

^c Justus-Liebig-University Gießen, Center for Materials Research (ZfM), Heinrich-Buff-Ring 17, 35392 Gießen, Germany

^d Max Planck Institute for Solid State Research, Heisenbergstraße 1, 70569 Stuttgart, Germany

^e Delft University of Technology, Department of Radiation Science and Technology, Mekelweg 15, Delft 2629JB, The Netherlands

^f University of Stuttgart, Institute for Materials Science, Materials Design, Pfaffenwaldring 55, 70569 Stuttgart, Germany

^g Ludwig-Maximilians-Universität München, Department of Chemistry, Butenandtstraße 5-13, 81377 München, Germany

^h University of Stuttgart, Institute for Materials Science, Chemical Materials Synthesis, Heisenbergstraße 3, 70569 Stuttgart, Germany

Corresponding Author:

Dr. Kerstin Wissel

Email: kerstin.wissel@tu-darmstadt.de

Fax: +49 6151 16-21991

Table S 1: Physical and chemical properties of solvents used in this study. ¹ Additionally, the water contents of the solvents after drying as determined from Karl-Fischer titration are given as a mean of three measurements.

Solvent	Classification	Dielectric constant ϵ_r	Polarity index	Boiling point T_{bp} [°C]	Water content after drying [ppm]
Hexane	Non-polar	1.88	0.009	68.7	Not detectable
Toluene	Non-polar	2.38	0.099	110.6	6.2
Tetrahydrofuran	Aprotic, polar	7.58	0.207	66.0	79.7
Ethyl acetate	Aprotic, polar	6.02	0.228	77.2	18.6
1,2-Dimethoxyethane	Aprotic, polar	7.20	0.231	84.6	12.7
Acetonitril	Aprotic, polar	35.94	0.460	81.6	88.8
N-Methylformamide	Protic, polar	182.40	0.722	200	17.7
Isoproponal	Protic, polar	19.92	0.546	82.2	58.3
Ethanol	Protic, polar	24.55	0.654	78.3	147.0
Methanol	Protic, polar	32.66	0.762	64.5	99.2

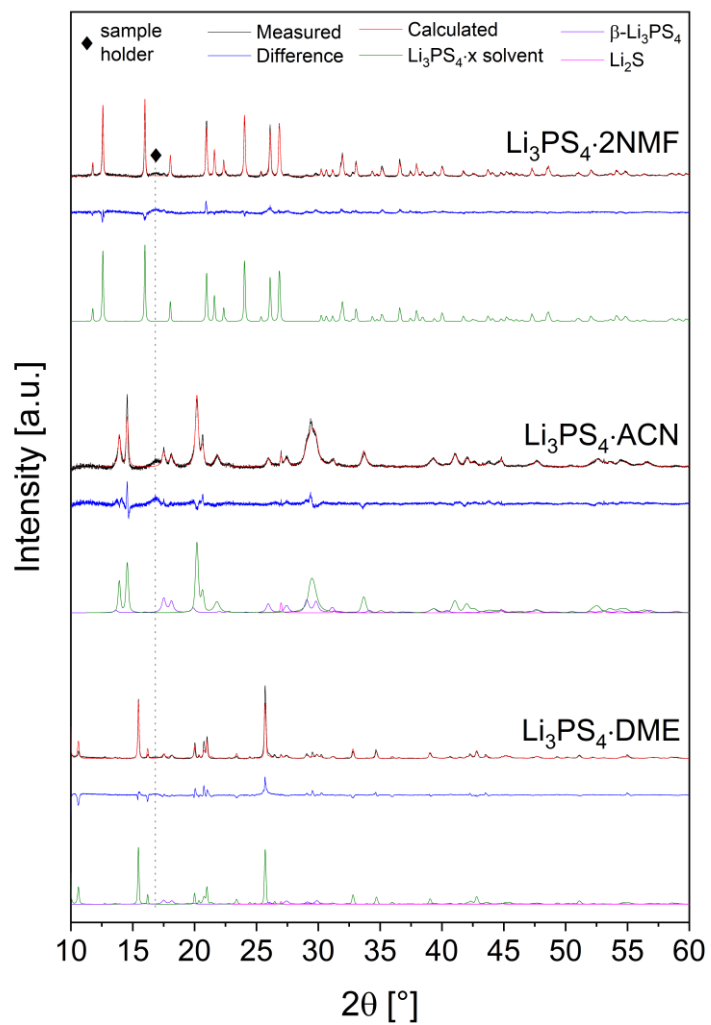


Figure S1: Rietveld refinements of complexes $\text{Li}_3\text{PS}_4 \cdot \text{DME}$, $\text{Li}_3\text{PS}_4 \cdot \text{ACN}$ and complexes $\text{Li}_3\text{PS}_4 \cdot 2\text{NMF}$ obtained after solvent removal at 120 °C for 4 h under reduced pressure.

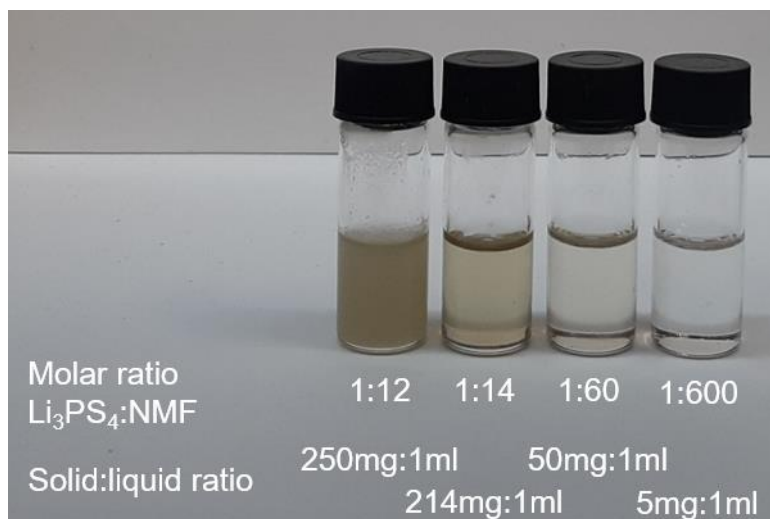


Figure S2: Photograph of $\beta\text{-Li}_3\text{PS}_4$ in NMF when using different molar or liquid-to-solid ratios of $\beta\text{-Li}_3\text{PS}_4$ to NMF.

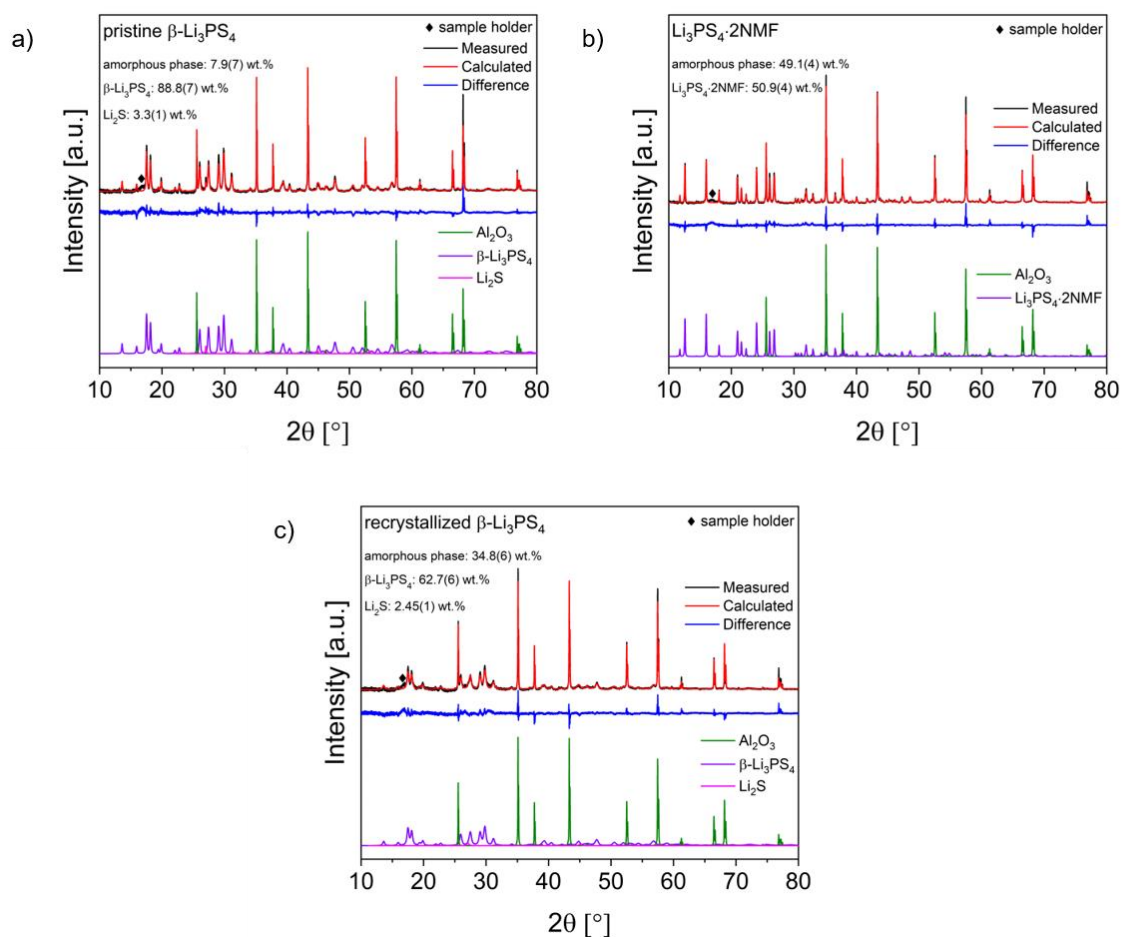


Figure S3: Rietveld refinements of pristine $\beta\text{-Li}_3\text{PS}_4$, $\text{Li}_3\text{PS}_4 \cdot 2\text{NMF}$ and recrystallized $\beta\text{-Li}_3\text{PS}_4$ mixed with 50 wt. % Al_2O_3 . From this, using the internal standard method, amorphous phase fractions were determined.

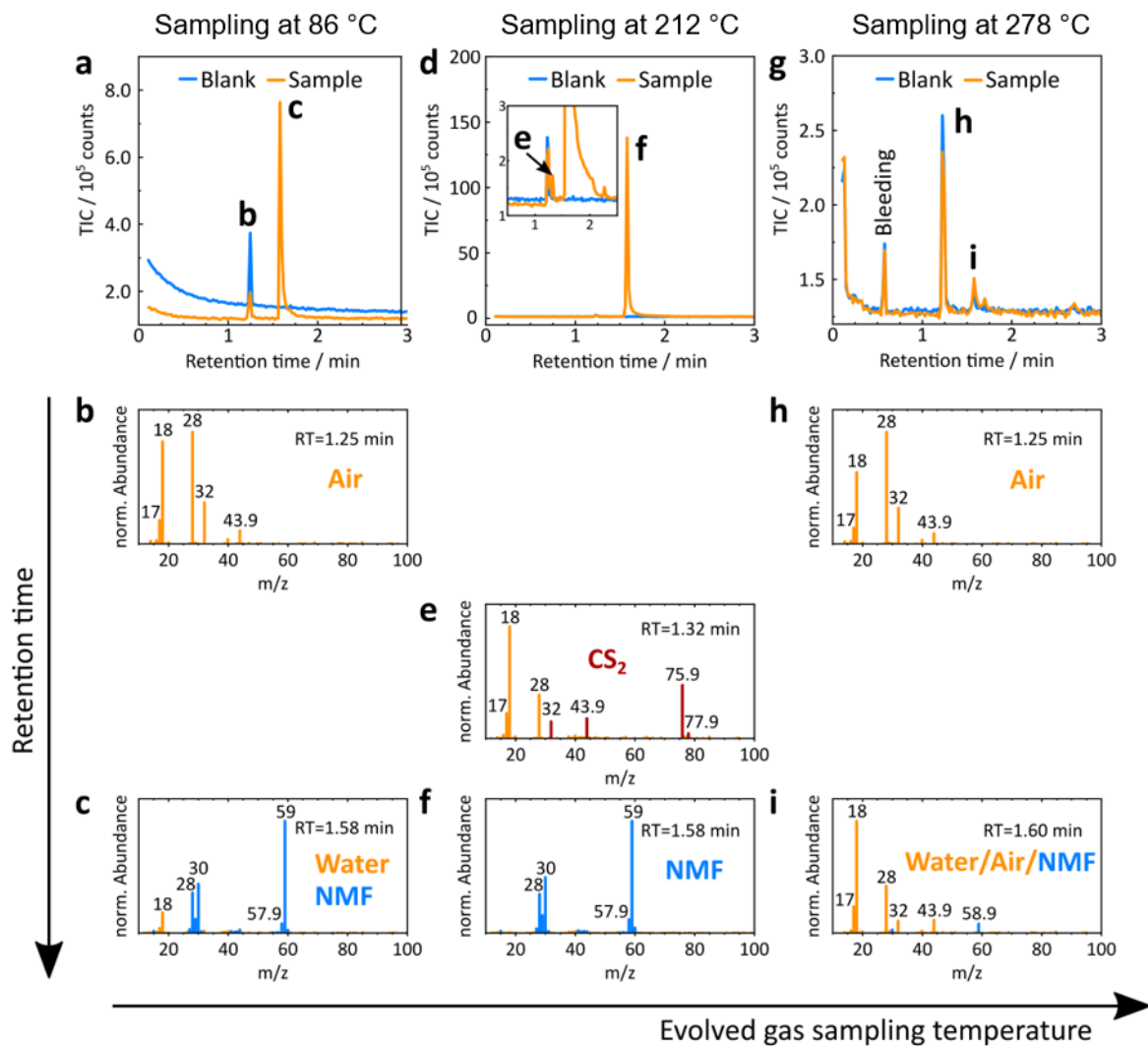


Figure S4: Evolving gas analysis at sampling temperatures of 86, 212 and 278 °C in dependence of the retention time.

Table S2: Structural parameters of $\text{Li}_3\text{PS}_4\cdot 2\text{NMF}$ optimized in the DFT simulation.

Atom	Wyckoff position	x	y	z	Occupancy
Li1	4e	0	0.35097039	3/4	1
Li2	8f	0.82862866	0.18275187	0.07521074	1
P1	4e	0	0.85005548	3/4	1
S1	8f	0.88733482	0.04838892	0.71203580	1
S2	8f	0.01907986	0.65154727	0.85591918	1
C1	8f	0.60590423	0.72475676	0.02173654	1
C2	8f	0.69529914	0.41210385	0.11013639	1
H1	8f	0.71702934	0.31900926	0.17289997	1
H2	8f	0.61810518	0.59983487	0.14608463	1
H3	8f	0.66208918	0.78031623	0.01009642	1
H4	8f	0.57411478	0.86618704	0.03581852	1
H5	8f	0.55537664	0.64208459	0.96064680	1
N1	8f	0.63972411	0.57817329	0.09881187	1
O1	8f	0.72318715	0.36013462	0.05485593	1

a [Å] 16.67252033 **b** [Å] 6.08178941 **c** [Å] 16.90241299 **β** [°] 118.09445339

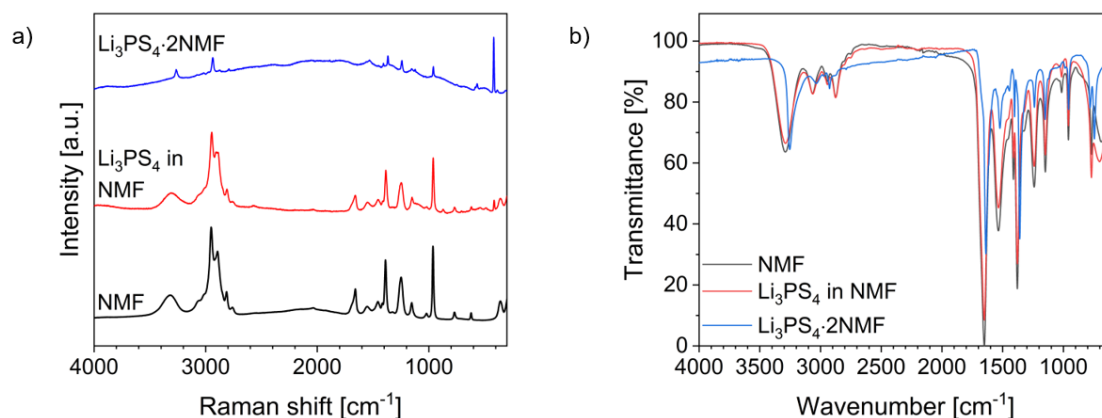


Figure S5: Raman (a) and FTIR (b) spectra of NMF, $\beta\text{-Li}_3\text{PS}_4$ dissolved in an excess of NMF and $\text{Li}_3\text{PS}_4\cdot 2\text{NMF}$. The Raman spectrum of $\beta\text{-Li}_3\text{PS}_4$ dissolved in an excess of NMF is dominated by the spectra of NMF, nevertheless the signal at $\sim 421\text{ cm}^{-1}$ corresponding to PS_4^{3-} is still visible, indicating that the ortho-thiophosphate units remain intact in solution. Only after the removal of the excess NMF, the PS_4^{3-} signal becomes dominant. A similar observation can be made for the FTIR spectra where also only after the removal of excess NMF, significant shifts in the bands are observed which correspond well to the observed interactions between Li_3PS_4 and NMF in $\text{Li}_3\text{PS}_4\cdot 2\text{NMF}$.

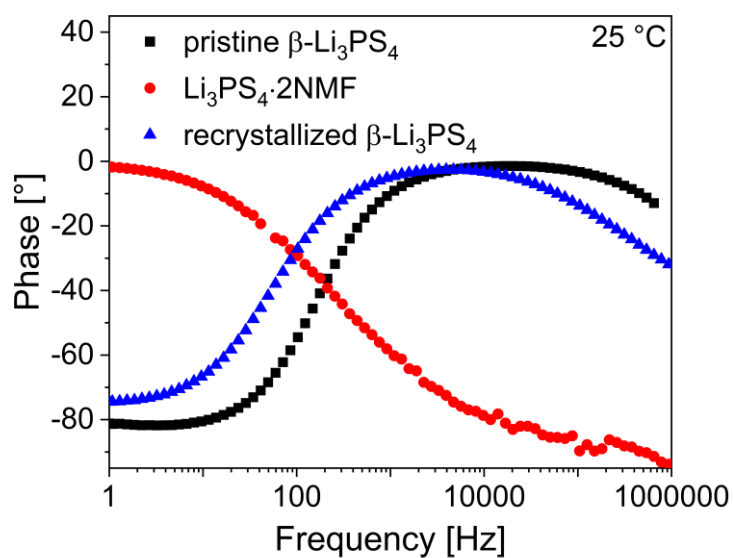


Figure S6: Bode plots of pristine β - Li_3PS_4 , $\text{Li}_3\text{PS}_4 \cdot 2\text{NMF}$ and recrystallized β - Li_3PS_4 .

References

1. Appendix A. Properties, Purification, and Use of Organic Solvents. In *Solvents and Solvent Effects in Organic Chemistry*, 2010; pp 549-586.